



HAL
open science

Individual and joint inversion of head and flux data by geostatistical hydraulic tomography

Behzad Pouladi, Niklas Linde, Laurent Longuevergne, Olivier Bour

► To cite this version:

Behzad Pouladi, Niklas Linde, Laurent Longuevergne, Olivier Bour. Individual and joint inversion of head and flux data by geostatistical hydraulic tomography. *Advances in Water Resources*, 2021, 154, pp.103960. 10.1016/j.advwatres.2021.103960 . insu-03236469

HAL Id: insu-03236469

<https://insu.hal.science/insu-03236469>

Submitted on 26 May 2021

HAL is a multi-disciplinary open access archive for the deposit and dissemination of scientific research documents, whether they are published or not. The documents may come from teaching and research institutions in France or abroad, or from public or private research centers.

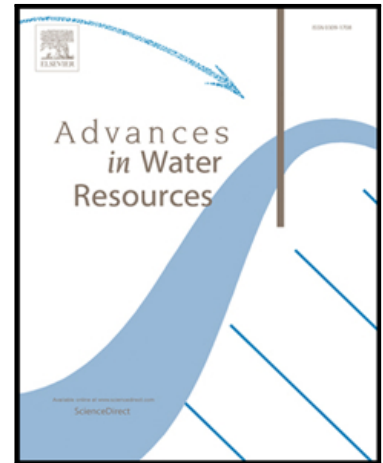
L'archive ouverte pluridisciplinaire **HAL**, est destinée au dépôt et à la diffusion de documents scientifiques de niveau recherche, publiés ou non, émanant des établissements d'enseignement et de recherche français ou étrangers, des laboratoires publics ou privés.

Journal Pre-proof

Individual and joint inversion of head and flux data by geostatistical hydraulic tomography

Behzad Pouladi , Niklas Linde , Laurent Longuevergne ,
Olivier Bour

PII: S0309-1708(21)00115-9
DOI: <https://doi.org/10.1016/j.advwatres.2021.103960>
Reference: ADWR 103960



To appear in: *Advances in Water Resources*

Received date: 5 February 2021
Revised date: 17 May 2021
Accepted date: 17 May 2021

Please cite this article as: Behzad Pouladi , Niklas Linde , Laurent Longuevergne , Olivier Bour , Individual and joint inversion of head and flux data by geostatistical hydraulic tomography, *Advances in Water Resources* (2021), doi: <https://doi.org/10.1016/j.advwatres.2021.103960>

This is a PDF file of an article that has undergone enhancements after acceptance, such as the addition of a cover page and metadata, and formatting for readability, but it is not yet the definitive version of record. This version will undergo additional copyediting, typesetting and review before it is published in its final form, but we are providing this version to give early visibility of the article. Please note that, during the production process, errors may be discovered which could affect the content, and all legal disclaimers that apply to the journal pertain.

© 2021 Published by Elsevier Ltd.

Individual and joint inversion of head and flux data by geostatistical hydraulic tomography

Behzad Pouladi^{1,*}, Niklas Linde², Laurent Longuevergne¹, Olivier Bour¹

¹Univ Rennes, CNRS, Géosciences Rennes, UMR 6118, 35000 Rennes, France

²University of Lausanne, Institute of Earth Sciences, Lausanne, Switzerland

*Corresponding author.

Highlights

- Geostatistical inversion of head and flux data recorded under steady-state conditions
- For few observations, flux data is more informative than head data
- For many observations, the inversion results are comparable regardless of data type
- For equal number of observations, individual and joint inversion perform similarly
- The pumping borehole boundary condition affects individual, but not joint inversion

ABSTRACT

Hydraulic tomography is a state-of-the-art method for inferring hydraulic conductivity fields using head data. We employed geostatistical inversion using synthetically generated head and flux data individually and jointly in a steady-state experiment. We designed 96 inversion scenarios to better understand the relative merits of each data type. For the typical case of a small number of observation points, we find that flux data provide a better resolved hydraulic conductivity field compared to head data when considering data with similar signal-to-noise ratios. This finding is further confirmed by a resolution analysis. When considering a high number of observation points, the estimated fields are of

26 similar quality regardless of the data type. In terms of borehole boundary conditions, the best setting for
27 flux and head data are constant head and constant rate, respectively, while joint inversion results are
28 insensitive to the borehole boundary type. When considering the same number of observations, the
29 joint inversion of head and flux data does not offer advantages over individual inversions. When
30 considering the same number of observation points and, hence, twice as many observations, the joint
31 inversion performs better than individual inversions. The findings of this paper are useful for future
32 planning and design of hydraulic tomography tests comprising flux and head data.

33

34 **KEYWORDS**

35 hydraulic tomography, groundwater flux, geostatistical inversion, principal component geostatistical
36 analysis (PCGA), resolution analysis

37 **1. INTRODUCTION**

38 Knowledge of hydraulic conductivity distributions is essential for the management of water
39 resources (Liu et al., 2020), solute transport predictions (Yeh, 1992; Jiménez, 2015) and designing
40 remediation of contaminated sites (Fakhreddine et al., 2016). A variety of geophysical (Kowalsky et al.,
41 2004; Revil et al., 2012; Slater, 2007) and hydraulic methods (Brauchler et al., 2003; Yeh and Liu, 2000;
42 Zhu and Yeh, 2005), including tracer-based measurements (Doro et al., 2015; Jiménez et al., 2016;
43 Somogyvári and Bayer, 2017), have been developed and employed for characterizing hydraulic
44 properties (Lochbühler et al., 2013). In hydraulic flow methods, head data responses to hydraulic
45 perturbations (pumping, tidal fluctuation, etc.) are measured at different locations across the aquifer.
46 The recorded head data are then used to estimate the spatial distribution of hydraulic conductivity (K)
47 and storativity. A distinct advantage of hydraulic methods for imaging purposes is that the hydraulic
48 response of an aquifer is directly related to its hydraulic parameters described by flow equations
49 (Fakhreddine et al., 2016), while in most geophysical methods, the hydraulic properties are indirect and
50 inferred from other estimated physical properties, thereby, requiring petrophysical relationships. We
51 define $Y = \log_{10}(K)$ and assume that it can be described by a stationary multivariate Gaussian distribution.
52 In other words, Y is the log₁₀ based hydraulic conductivity field.

53 Hydraulic tomography is one type of hydraulic method and has been the subject of many theoretical
54 and numerical studies (Fienen et al., 2008; Luo et al., 2020; Yeh and Liu, 2000; Zha et al., 2018; Zhu and
55 Yeh, 2005), laboratory experiments (Illman et al., 2008, 2010; Liu et al., 2002, 2007; Yin and Illman,
56 2009; Zhao et al., 2016), and field studies (Berg and Illman, 2015, 2013, 2011; Bohling et al., 2007;
57 Brauchler et al., 2013, 2011, 2010, 2003; Cardiff et al., 2009, 2013; Cardiff and Barrash, 2011; Fischer et
58 al., 2017; Gottlieb and Dietrich, 1995; Huang et al., 2011; Klepikova et al., 2013; Kuhlman et al., 2008;
59 Paradis et al., 2016, 2015; Sun et al., 2013; Tosaka et al., 1993). However, hydraulic tomography based
60 on head data alone has limitations. One limitation is inherent to the underlying potential-field physics as
61 measured head data are spatially averaged due to the diffusive nature of pressure disturbances created
62 during the test (Bohling and Butler Jr, 2010). This averaging results in tomographic estimates displaying a
63 high degree of smoothing compared to the actual aquifer property fields. This smearing may lead to

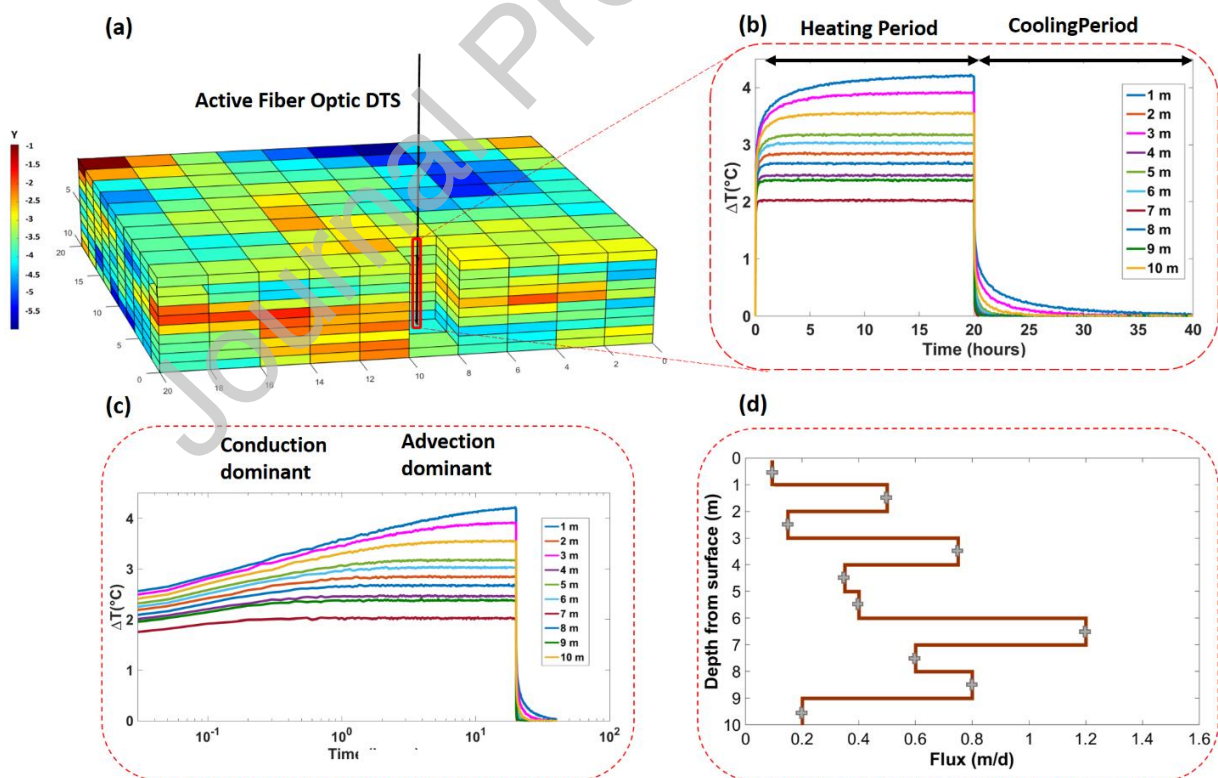
64 degraded predictions for transport problems. It should be noted that the smoothing would only appear
65 in a single, regularized solution. However, if one uses stochastic methods, one should be able to
66 represent the stochastic nature of the underlying actual aquifer property fields. Furthermore, some
67 authors have included geological data as a priori information to overcome this issue (Luo et al., 2017;
68 Zha et al., 2017; Zhao and Illman, 2018). Another limitation appears in applying hydraulic tomography in
69 high conductivity aquifers as hydraulic tests lead to small drawdown values, implying high relative
70 uncertainty of the measured head perturbations and correspondingly low signal-to-noise ratio data.
71 Adding other types of non-redundant data in hydraulic tomography can help to better image the
72 subsurface (Mao et al., 2013; Yeh et al., 2015). In this regard, Zha et al. (2014) demonstrated the
73 usefulness of flux data (specific discharge) for hydraulic tomography in a 2D synthetic fractured media
74 mimicking a field site in Mizunami, Japan. Estimated mean, variance, and correlation length of the Y -
75 field were applied as prior information to the inversion model. Using the cross-correlation approach
76 (Zha et al., 2014), they showed that head and flux contribute differently to the Y -field reconstruction.
77 They claimed that inversion of head data collected with known pumping rate can result in
78 representative Y -field estimates even if the initial guess is incorrect. For flux data, they find that the final
79 Y -field estimate is dependent on the initial guess. Their synthetic work showed that using flux data with
80 head data improves the estimation of Y -field values and the fracture distribution. In another study, Tso
81 et al. (2016) performed numerical test studies on a 3D model mimicking the aquifer at the North
82 Campus Research site in Waterloo, Canada. They simulated pumping in this porous aquifer and
83 measured head data and flux data at different locations. Then, head and flux data were subjected to
84 inversion, considering different types of prior information. They showed that using flux data jointly with
85 head data can enhance hydraulic conductivity estimates. Furthermore, they found out that the
86 estimated hydraulic conductivity field is less affected by an inadequate prior model when non-
87 redundant flux data are used to supplement the head data.

88 Until recently, measurements of groundwater fluxes in the field were limited to local and time-
89 consuming measurements. The most popular technique for quantifying groundwater flux in the field
90 was based on dilution tests (Drost et al., 1968; Jamin et al., 2015; Schneider et al., 2019), where the
91 dilution of an injected tracer inside a screened borehole or within packers is used to estimate the
92 horizontal groundwater flux. Other approaches, such as the colloidal borescope (Kearl, 1997), the point
93 velocity probe (Labaky et al., 2007) or the in-situ permeable flow sensor (Ballard, 1996), can also
94 measure the horizontal groundwater flux. A comprehensive review of the groundwater velocity
95 measurement approaches is provided by Devlin (2020). Nevertheless, boreholes disturb the flow field
96 and affect the measurements; hence, the measured values may not represent the real flux values.
97 Moreover, these methods are in general limited to local measurements and do not provide in most
98 cases the spatial variability of groundwater fluxes.

99 The recent advent of Fiber Optic Distributed Temperature Sensors (FO-DTS) has led to new
100 possibilities for measuring groundwater discharge with unprecedented spatial resolution (des Tombe et
101 al., 2019; Simon et al., 2021, del Val et al., 2021). FO-DTS is a distributed sensor type that allows
102 measurements of temperature all along the fiber optic cable. FO-DTS can be employed in both passive
103 and active modes. In passive mode, the temperature of the fiber optic is measured without any external

104 forcing, while in active mode, a heat source is added to the fiber optic cable by using a heating element
 105 located very close to the fiber optic cable or by using a heating fiber optic cable. Active-DTS have been
 106 developed, for instance, for measuring borehole flows (Read et al., 2014), wind speed (Sayde et al.,
 107 2015), and for characterizing groundwater fluxes in fractured media (Maldaner et al., 2019). Recently, it
 108 has also been used for measuring groundwater discharge in sedimentary aquifers; the FO cable typically
 109 being installed by the direct push method (Bakker et al., 2015; des Tombe et al., 2019) or along
 110 boreholes (del Val et al., 2021). In this case, the buried cable is in direct contact with the ground with
 111 minimum subsurface perturbations. Simon et al. (2021) showed that active-DTS can be used for
 112 measuring both sediment thermal conductivities and groundwater fluxes on a large range of values with
 113 excellent accuracy (with errors of less than 10% for groundwater flux in the range of 10^{-5} to 10^{-3} m/s).
 114 The principle of such an experiment (Figure 1) is to monitor the temperature evolution with time, which
 115 depends on the surrounding area's thermal properties and also groundwater fluxes that limits the
 116 temperature rise. Typically, the slope of the temperature rise in the conduction regime (with time in
 117 logarithmic scale) is inversely proportional to thermal conductivity while the greater the groundwater
 118 fluxes, the lower the temperature at stabilization. The temperature evolution with time may be easily
 119 interpreted to estimate groundwater fluxes through an analytical solution or by using a graphical
 120 analysis (Simon et al., 2021). The application of Active FO-DTS for flux measurements is currently limited
 121 to shallow and unconsolidated aquifers due to limitations in deployment by the direct push method.

122



123

124 **Figure 1:** Schematic description of how Active FO-DTS can be used to infer a groundwater flux profile
 125 with depth. **(a)** An Active Fiber Optic Cable is deployed vertically into the ground in close contact with
 126 the formation. **(b)** The cable is heated (active mode), and the cable temperature during the heating (first
 127 20 hours) and cooling periods (from 20 to 40 hours) is measured. Each curve corresponds to one-point
 128 measurement along the FO-cable. **(c)** In semi-logarithmic plot, the slope of the temperature profile is
 129 used to estimate the thermal conductivity while the temperature at stabilization is dependent on
 130 groundwater fluxes (Simon et al., 2021). **(d)** Measured temperature data along the fiber optic cable are
 131 converted to a flux profile with depth, with each "+" sign indicate one datum.

132

133 New advances in distributed sensing of local groundwater flux make it an appealing data source for
 134 independent inversion or joint inversion with hydraulic head. This present study assumes that
 135 groundwater fluxes can be inferred from such above-mentioned techniques at a prescribed spatial
 136 resolution and accuracy. It is worth mentioning that measuring head data is more accurate and easier
 137 than flux data. However, Active FO-DTS and new developments in the data analysis provide promising
 138 result for measurement of the flux along FO cables. Here, we limit ourselves to a 2-D study assuming
 139 constant groundwater flux in depth. Using a geostatistical hydraulic tomography approach, we then
 140 address the benefits and drawbacks of using either head or flux data individually or jointly. More
 141 specifically, we address the following questions.

142 (1) For an equal number and locations of flux and head data, which data type leads to the best
 143 reconstruction of hydraulic conductivity?

144 (2) How does the number of observations affect the inversion results?

145 (3) How does inversion performance for the different data types vary with the hydraulic conductivity
 146 field variance?

147 The paper is structured into six sections. Section 2 presents the geostatistical inversion method and
 148 the forward model employed. In section 3, we describe the hydraulic conductivity test model used for
 149 our analysis. In sections 4 and 5, we present and discuss the main results, respectively, and section 6
 150 concludes the paper.

151 2. METHODS

152 The Principal Component Geostatistical Approach (PCGA) is a computationally-efficient geostatistical
 153 inversion method (Lee and Kitanidis, 2014). PCGA uses the main principal components of the prior
 154 model covariance matrix for model parameterization and corresponding estimates of the Jacobian
 155 (sensitivity matrix). The resulting model reduction from a model of many gridded elements to a lower
 156 number of retained principal components leads to smaller matrices to invert and fewer sensitivities to
 157 estimate, implying less computational costs than full inversions. This method has been employed
 158 extensively in recent years (Fakhreddine et al., 2016; Fischer et al., 2017; Kang et al., 2017; Lee et al.,

159 2018; Soueid Ahmed et al., 2016). In this study, we use PCGA combined with the Matlab Reservoir
 160 Simulation Toolbox (MRST) that simulates fluid flow in porous media (forward model) to perform
 161 inversion of head and flux data.

162 2.1 Inverse model

163 Inferring properties of subsurface media (storage, hydraulic conductivity) from error-contaminated
 164 and sparse observed data (head data, flux data, etc.) is an inverse problem and can be formulated as
 165 follow:

$$\mathbf{d} = f(\mathbf{m}) + \boldsymbol{\eta}, \quad (1)$$

166 where \mathbf{d} , $f(\cdot)$, \mathbf{m} and $\boldsymbol{\eta}$ refer to measured data, forward model, model parameters and errors,
 167 respectively. The forward model refers here to a non-linear operator solving a set of differential
 168 equations numerically to describe the relationship between model parameters and data. When
 169 considering the joint inversion of two different data type (\mathbf{d}_1 and \mathbf{d}_2), the formulation is as follow:

$$\begin{bmatrix} \mathbf{d}_1 \\ \mathbf{d}_2 \end{bmatrix} = f(\mathbf{m}) + \begin{bmatrix} \boldsymbol{\eta}_1 \\ \boldsymbol{\eta}_2 \end{bmatrix}, \quad (2)$$

170 From a mathematical point of view, the inverse problem is often ill-posed and the solution is non-
 171 unique, implying that additional information (e.g., a prior model) is required to obtain unique and
 172 physically-meaningful results. The prior model inferred based on the available information about the
 173 subsurface media. In this work, the same prior model is used throughout to avoid the effect of the prior
 174 model on the comparisons of final results. Here, the subsurface is described as a multi-Gaussian
 175 stationary field with known statistical properties and a superimposed deterministic trend. In the
 176 presence of a multivariate Gaussian prior model and error distribution, it is common to formulate the
 177 inverse problem in terms of an exploration of the maximum a posteriori (MAP) estimate and its
 178 variance. In such a setting, the solution of the inverse problem is obtained by maximizing a posterior
 179 probability density function (maximizing the term in bracket) expressed by using Bayes' theorem as
 180 follow:

$$\pi_{post}(\mathbf{m}|\mathbf{d}) \sim \exp\left[-\frac{1}{2}(\mathbf{f}(\mathbf{m}) - \mathbf{d})\mathbf{C}_d^{-1}(\mathbf{f}(\mathbf{m}) - \mathbf{d}) + \frac{1}{2}(\mathbf{m} - \mathbf{m}_{prior})\mathbf{C}_m^{-1}(\mathbf{m} - \mathbf{m}_{prior})\right], \quad (3)$$

181 where \mathbf{C}_m and \mathbf{C}_d are the a priori model covariance and data covariance matrix, respectively (Kitanidis,
 182 1995).

183 Geostatistical methods have been widely used and proven to be efficient for hydraulic tomography
 184 purposes (Illman et al., 2015). The iterative optimization process estimates the model parameters. The
 185 solution at $(i+1)^{th}$ iteration is calculated as:

$$\mathbf{m}_{i+1} = \mathbf{X}\boldsymbol{\beta}_i + \mathbf{C}_m \mathbf{J}_i^T \boldsymbol{\epsilon}_i, \quad (4)$$

186 where \mathbf{X} is a known matrix, and $\boldsymbol{\beta}$ is an unknown vector used to determine linear trends that is inferred
 187 along with $\boldsymbol{\epsilon}$ by solving the system of equations below. In this equation, \mathbf{X} is a trend matrix and $\boldsymbol{\beta}$ is trend

188 vector. Here \mathbf{J} represents the Jacobian matrix describes the sensitivity of the forward model output (at
 189 observation points) with respect to the unknown model parameters.

$$\begin{bmatrix} \mathbf{J}_i \mathbf{C}_m \mathbf{J}_i^T + \mathbf{C}_d & \mathbf{J}_i \mathbf{X} \\ (\mathbf{J}_i \mathbf{X})^T & 0 \end{bmatrix} \begin{bmatrix} \boldsymbol{\varepsilon}_i \\ \boldsymbol{\beta}_i \end{bmatrix} = \begin{bmatrix} \mathbf{d} - f(\mathbf{m}_i) + \mathbf{J}_i \mathbf{m}_i \\ 0 \end{bmatrix}. \quad (5)$$

190 2.1.1 Principal Component Geostatistical Approach

191 Calculating the Jacobian matrix (\mathbf{J}) used in equations (4) and (5) for high-dimensional problems often
 192 requires a very high computational effort. Lee and Kitandis (2014) proposed the Principal Component
 193 Geostatistical Approach (PCGA), which uses a low-rank approximation of the prior covariance via
 194 principal component analysis and avoids forming the Jacobian explicitly for products of the Jacobian
 195 matrix and eigenvalues (equations (7) and (8)) by using a finite difference approximation (equation (9)).
 196 This results in a faster inversion process of high accuracy, provided that an adequate number of principal
 197 components are retained. The terms that are used for geostatistical inversion in equation (5) are
 198 approximated through the P largest principal components as follow:

$$\mathbf{C}_m \approx \mathbf{C}_{mP} = \sum_{ii=1}^P (\boldsymbol{\varsigma}_{ii})(\boldsymbol{\varsigma}_{ii})^T, \quad (6)$$

$$\mathbf{J}_i \mathbf{C}_m \approx \mathbf{J}_i \mathbf{C}_{mP} = \mathbf{J}_i (\mathbf{Z})(\mathbf{Z})^T = \mathbf{J}_i \sum_{ii=1}^P (\boldsymbol{\varsigma}_{ii})(\boldsymbol{\varsigma}_{ii})^T = \sum_{ii=1}^P (\mathbf{J}_i \boldsymbol{\varsigma}_{ii})(\boldsymbol{\varsigma}_{ii})^T, \quad (7)$$

$$\mathbf{J}_i \mathbf{C}_m \mathbf{J}_i^T \approx \mathbf{J}_i \mathbf{C}_{mP} \mathbf{J}_i^T = \sum_{ii=1}^P (\mathbf{J}_i \boldsymbol{\varsigma}_{ii})(\mathbf{J}_i \boldsymbol{\varsigma}_{ii})^T, \quad (8)$$

$$\mathbf{J}_i \boldsymbol{\varsigma}_{ii} \approx \frac{1}{\delta} [f(\mathbf{m}_i + \delta \boldsymbol{\varsigma}_{ii}) - f(\mathbf{m}_i)]. \quad (9)$$

199 Here, \mathbf{C}_{mP} is a rank- P approximation of the model parameter covariance matrix. The \mathbf{C}_{mP} and Jacobian
 200 matrix products required for the inversion (equation 5) are given by equations (7)-(8). \mathbf{Z} is a $m \times p$ matrix
 201 and $\boldsymbol{\varsigma}_{ii}$ is the i^{th} column vector of \mathbf{Z} . How to choose the finite difference interval δ is addressed by Lee
 202 and Kitandis (2014).

203 The diagonal entries of the posterior covariance matrix (\mathbf{v}_{jj}) are often presented as the estimation of
 204 the variance and can be calculated without explicit construction of \mathbf{v} (Lee and Kitanidis, 2014)

$$\mathbf{v}_{jj} = \mathbf{C}_{mjj} - \begin{bmatrix} (\mathbf{J}\mathbf{C}_m)_j \\ \mathbf{X}^T \end{bmatrix}^T \begin{bmatrix} \mathbf{J}\mathbf{C}_m \mathbf{J}^T + \mathbf{C}_d & \mathbf{J}\mathbf{X} \\ (\mathbf{J}\mathbf{X})^T & 0 \end{bmatrix}^{-1} \begin{bmatrix} (\mathbf{J}\mathbf{C}_m)_j \\ \mathbf{X}_j^T \end{bmatrix}, \quad (10)$$

205 where \mathbf{C}_{mjj} represents the j^{th} diagonal entry of the model covariance matrix and $(\mathbf{J}\mathbf{X})_j$ is the j^{th} column of
 206 the product $\mathbf{J}\mathbf{X}$. In this work, Levenberg–Marquardt algorithm (by introducing a multiplier to the error
 207 matrix for dampening) is used to reduce the distance between simulation and observation.

208
 209 Once the model parameters are determined, it is desirable to perform a resolution analysis by
 210 obtaining the resolution matrix (\mathbf{R}), which can be seen as a low pass filter that maps the true model

211 parameters to the estimated model parameters (e.g., Alumbaugh and Newman, 2000). Each model
 212 parameter during the inversion is estimated from the averaging of other model parameters adjacent to
 213 the one of interest. The components of \mathbf{R} can be interpreted as weights (each row in the resolution
 214 matrix) of the average of true model parameters for estimating each model parameter (Day-Lewis et al.,
 215 2005). The ideal resolution matrix would be an identity matrix that would imply that all model
 216 parameters are resolved perfectly. The deviation of the diagonal element from the identity matrix
 217 reveals the degree of averaging and smoothness. Thus, plotting diagonal elements of the resolution
 218 matrix in their corresponding blocks is indicative of the degree of smoothness. The diagonal elements of
 219 the resolution matrix (equation 11) inform the extent to which each estimated parameter is resolved
 220 independently.

221 The resolution matrix (\mathbf{R}) is obtained by equation (12), which requires recovering the Jacobian matrix
 222 (\mathbf{J}_r) from the previously calculated product (equation 7) and inverse of low rank-approximation of the
 223 covariance matrix (\mathbf{C}_{mp}) as shown in equation (13);

$$224 \quad \mathbf{m}^{\text{estimate}} = \mathbf{R}\mathbf{m}^{\text{true}}, \quad (11)$$

$$\mathbf{R} = (\mathbf{J}_r^T(\mathbf{C}_d)^{-1}\mathbf{J}_r)^{-1}(\mathbf{J}_r^T(\mathbf{C}_d)^{-1}\mathbf{J}_r). \quad (12)$$

$$\mathbf{J}_r = \left(\sum_{ii=1}^P (\mathbf{J}_i \mathbf{s}_{ii})(\mathbf{s}_{ii})^T \right) \left(\sum_{ii=1}^P (\mathbf{s}_{ii})(\mathbf{s}_{ii})^T \right)^{-1} \quad (13)$$

225 It should be noted that \mathbf{J}_r is the Jacobian matrix mapped from the PCA space to the grid cells, while \mathbf{J} is
 226 the Jacobian matrix calculated directly for every principal component.

227 2.2 Forward model

228 The incompressible fluid flow module of MRST (Lie, 2019) was used to simulate steady-state
 229 groundwater flow. It is used to calculate head and flux values at different points across a confined
 230 aquifer. Starting from the mass conservation law on a control volume, introducing the Darcy law,
 231 assuming incompressible fluid flow and steady-state condition, the final form of the equation reads:
 232

$$233 \quad -\nabla \cdot [\mathbf{K}(\mathbf{w}) \cdot \nabla h(\mathbf{w})] = \mathbf{q}(\mathbf{w}), \quad (14)$$

234 subjected to the following constant head boundary conditions across external boundaries:

$$235 \quad h = h_D \quad \text{for } \vec{\mathbf{w}} \in \Gamma_a \quad (15)$$

236 Here, $\mathbf{w} = (x, y, z)$, K (L/T), h (L) and \mathbf{q} [L/T] represent the hydraulic conductivity, head and fluid source
 237 or sink (inflow or outflow of fluid per volume at certain locations), respectively. Γ_a represents Dirichlet
 238 boundaries. The above equations are solved numerically to calculate the head values at grid points
 239 across the aquifer. The MRST uses the two-point flux approximation scheme (Lie, 2019) to calculate the
 240 Darcy flux in each grid block. Starting from mass conservation, introducing the Darcy equation to the flux
 241 exchange at the face of a cell with its neighboring cells and imposing continuity of fluxes across all faces
 242 of a cell, the flux in each face (for instance in the x-direction) is calculated by:

$$\left[\frac{\Delta x_{cell}}{K_{cell}} + \frac{\Delta x_{neighbour}}{K_{neighbour}} \right]^{-1} (h_{cell} - h_{neighbour}) = v_{face}, \quad (16)$$

243 Here, Δx (L) is the length of the grid and v_{face} (L/T) is the fluid flux. This equation is solved for all other
 244 faces to obtain the flux in all faces. The value of the flux attributed to each cell is the Euclidean norm of
 245 flux in all faces.

246

247 3. NUMERICAL EXPERIMENTS

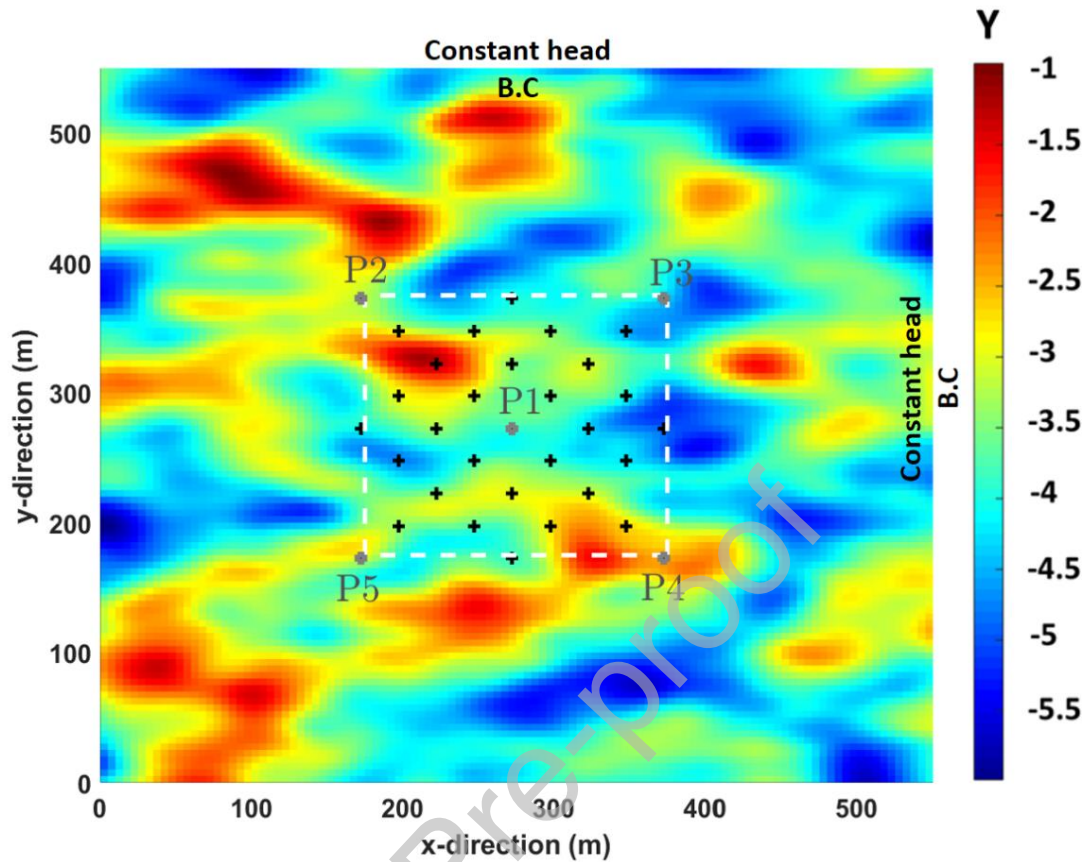
248 3.1 Setup of the synthetic test case

249 To assess the information content of hydraulic head and groundwater flux data for the
 250 reconstruction of heterogeneous aquifers, a stationary multi-Gaussian log-hydraulic conductivity field
 251 (with constant storativity) is generated using the fast circulant embedding technique, resulting in the
 252 field, shown in Figure 2. In this study, we consider steady-state hydraulic tomography in which
 253 storativity does not play a role in simulated head or flux data and can be considered as a constant value.
 254 The generated aquifer is 550 m in length, 550 m in width and 5 m in depth. The aquifer is discretized
 255 into $110 \times 110 \times 1$ in x -, y -, z - directions and corresponding block sizes are $5 \text{ m} \times 5 \text{ m} \times 5 \text{ m}$, respectively.
 256 The aquifer is assumed to have one layer, and the log-hydraulic conductivity field has a multi-Gaussian
 257 distribution. The area of interest is chosen in the middle of the aquifer, away from the boundaries to
 258 reduce the boundaries' effect on the inversion. All boundaries are set to a constant head equal to 350
 259 m.

260 The correlation length used for generating the Y -field is 75 m and 45 m for x - and y -directions,
 261 respectively. The same field (same heterogeneity structure) with different variances of 0.5, 1, 2, and 4
 262 are generated to assess the effect of variance and number of observations on the inversion results. The
 263 mean Y_{mean} is -3.57 for all cases, but the Y -fields variance and ranges are different for different
 264 experiments. This range of hydraulic conductivity is chosen to have measurable and realistic
 265 groundwater flux and head responses (both in real and synthetic aquifers).

266

267 We use a five-spot setup with a central borehole (P1) and four boreholes (P2, P3, P4 and P5) on the
 268 corners of the area of interest (bounded by white dashed lines in Figure 2). Other monitoring points are
 269 also considered between the boreholes, as shown by asterisk symbols. The aquifer is subjected to a
 270 series of pumping experiments in each borehole. The five boreholes are pumped sequentially (one at
 271 each time) and head/flux data are acquired in other boreholes and observation points. Two different
 272 boundary conditions in the borehole, namely, constant rate and constant head, are considered. When
 273 simulating pumping in one borehole, the head and flux values are recorded in other boreholes and
 274 monitoring points. The acquired flux and head data are noise-contaminated before being used to
 275 estimate the Y -field.



276

277 **Figure 2:** Reference Y-field (variance 4), borehole (P1 to P5), and monitoring locations (asterisks). All
 278 boundaries are set to the constant head. The white dash-lines crossing the side boreholes define the
 279 area of interest.

280

281 3.2 Hydraulic tomography using head and flux data

282 Our numerical inversion experiments aim to compare the relative merits of each data type and
 283 analyze how borehole boundary conditions (constant head or constant rate), the variance of the Y-field,
 284 and the number of observations affect the inversion results. The observational data are generated using
 285 the reference hydraulic conductivity field, and a normally distributed and independent error is added to
 286 the observations. The standard deviations of these errors are different in all cases. The errors' standard
 287 deviations were chosen to be in a realistic range while ensuring the same initial signal-to-noise ratio of
 288 38 for all cases defined by running the code using Y_{mean} . The resulting measurement errors range from
 289 0.05 to 0.013 (m) for the head and 0.055 to 0.01 (m/day) for the flux. The relation between values of
 290 groundwater flux and measurement uncertainty is provided by Simon et al. (2021). This relation was
 291 used to define a reasonable range of the noise model. It should be noted that the uncertainty depends
 292 highly on the range of flux measurements and the duration of the active-DTS experiments. Typically, for
 293 a relatively large range of values, the accuracy is very good, but for very high or very low flows values,

294 uncertainty is much greater (Simon et al., 2021). In this work, we assume that data quality in terms of
 295 signal-to-noise-ratio is the same for both head and flux data.

296 PCGA with previously mentioned geostatistical parameters (variance and correlation length) are
 297 used for the inversion. Increasing in the dimension of the problem results in massive computational
 298 needs. Considering the available computational methods, one may use the full covariance matrix, but if
 299 it is not possible, a sufficient number of components must be chosen to ensure that most of the
 300 heterogeneity features are captured. The truncation order (p -rank) of the prior covariance matrix is
 301 chosen as 400 out of 12100. Based on the recommendation by Lee et al. (2016), the truncation order (P),
 302 which results in the relative Eigenvalue error below 0.01 would be sufficient to capture most of the
 303 covariance matrix structure. The relative Eigenvalue error is defined as the ratio of first to ($P+1$)th
 304 Eigenvalue. We have chosen P more conservatively. For the Y -field with variance 4, the first Eigenvalue is
 305 1411.47, while the 401st Eigenvalue is 0.047 giving the ratio of 3.25×10^{-5} .

306 The inversion starts with a constant value of Y_{mean} and continues until the root mean square error
 307 between observed and simulated measurement, normalized with the error standard deviation
 308 (weighted root mean square error), defined in equation 15 reaches a value close to one,

$$\text{WRMSE} = \sqrt{\frac{\frac{1}{N} \sum_1^N (\mathbf{d} - f(\mathbf{m}^{\text{estimate}}))^2}{\sigma^2}}, \quad (15)$$

309 here N is the number of observations and σ is the absolute value of the error's standard deviation. If no
 310 convergence is obtained, the inversion ends after 10 iterations.

311

312 3.2.1 Boundary condition at the pumping borehole

313 The steady-state hydraulic tomography is simulated considering two different borehole boundary
 314 conditions: constant rate (the borehole is being pumped with constant flow rate) and constant head
 315 (the head in the borehole is kept constant). Note that the external boundary conditions do not change
 316 and are kept fixed. As an example, the pumping rates for the field case with variance 4 (Y -field variance)
 317 are 2400, 4000, 1750, 5000, and 3800 (m^3/day) for P1, P2, P3, P4, and P5, respectively. The equivalent
 318 constant head borehole boundary conditions are 324, 340, 300, 329 and 336 (m) for P1, P2, P3, P4, and
 319 P5, respectively. The inversion is performed on the whole domain but results are shown for the area of
 320 interest.

321

322 3.2.2 Variance of Y -field and number of observation points

323

324 The effect of the Y -field ($Y = \log_{10}(K)$) variance is investigated by considering four different variances
 325 (0.5, 1, 2 and 4). Furthermore, a different number of observation points are used to assess their impact
 326 on the final inversion results. The observation points are distributed symmetrically in the aquifer. The
 327 minimum number of observation points considered is the number of boreholes (4 observation points)
 328 and the maximum are the boreholes and the observation points shown by asterisks in Figure 2 (32
 329 observation points). We distinguish between the number of observations and the number of
 330 observation points. For head and flux data, the number of observation points and number of
 331 observations are the same. For joint inversion, the number of observations is twice the number of
 332 observation points.

333

334 **3.3 Performance Metrics**

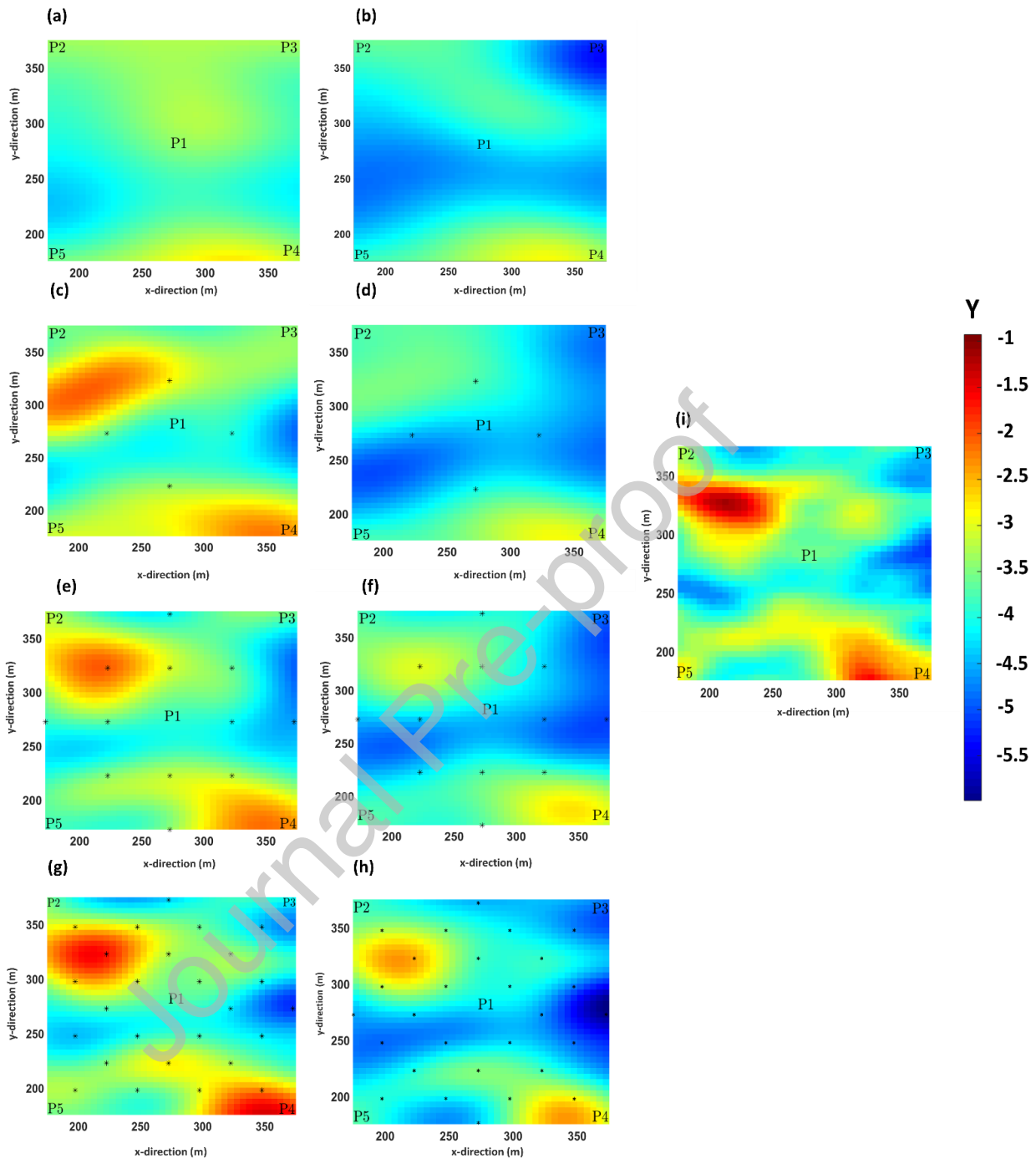
335 To evaluate each data type's performance in estimating Y , we use the Frobenius norm and scatter
 336 plots of estimated versus reference Y for each case. The Frobenius norm for the vector of difference
 337 between the reference Y and estimated Y is:

$$\text{Norm}^{\text{Fr}} = \sqrt{\sum_1^N |\mathbf{Y}_{\text{reference}} - \mathbf{Y}_{\text{estimated}}|^2}, \quad (16)$$

338 Furthermore, the correlation coefficient between reference Y and estimated Y -values and their
 339 corresponding slope lines are calculated. We stress that the comparison is based on the log of the
 340 hydraulic conductivity values and not the hydraulic conductivity itself, thereby, avoiding emphasizing
 341 large hydraulic conductivity values.

342 **4. RESULTS**343 **4.1 Inversion of head data**

344 First, the head data are individually inverted. The results are presented for 4 observation points
 345 (only the observations in the boreholes), 8, 16 and 32 observation points. For each case, two different
 346 borehole boundary conditions are considered: constant rate and constant head. Figure 3 shows the
 347 estimated Y -field with a variance of 4, and Table 1 represents the performance metrics.



348

349 **Figure 3:** Hydraulic conductivity field (variance 4) estimates from hydraulic head data: **(a)** inversion
 350 result for 4 observations point and constant rate B.C., **(b)** inversion result for 4 observations point and
 351 constant head B.C., **(c)** inversion result for 8 observations point and constant rate B.C., **(d)** inversion
 352 result for 8 observations point and constant head B.C., **(e)** inversion result for 16 observations point and
 353 constant rate B.C., **(f)** inversion result for 16 observations point and constant head B.C., **(g)** inversion

354 result for 32 observation points and constant rate B.C., (h) inversion result for 32 observation points and
 355 constant head B.C. (i) reference Y-field

356 **Table 1:** Performance metrics (in the area of interest) from the inversion of head data for the case of a Y-
 357 variance of 4.

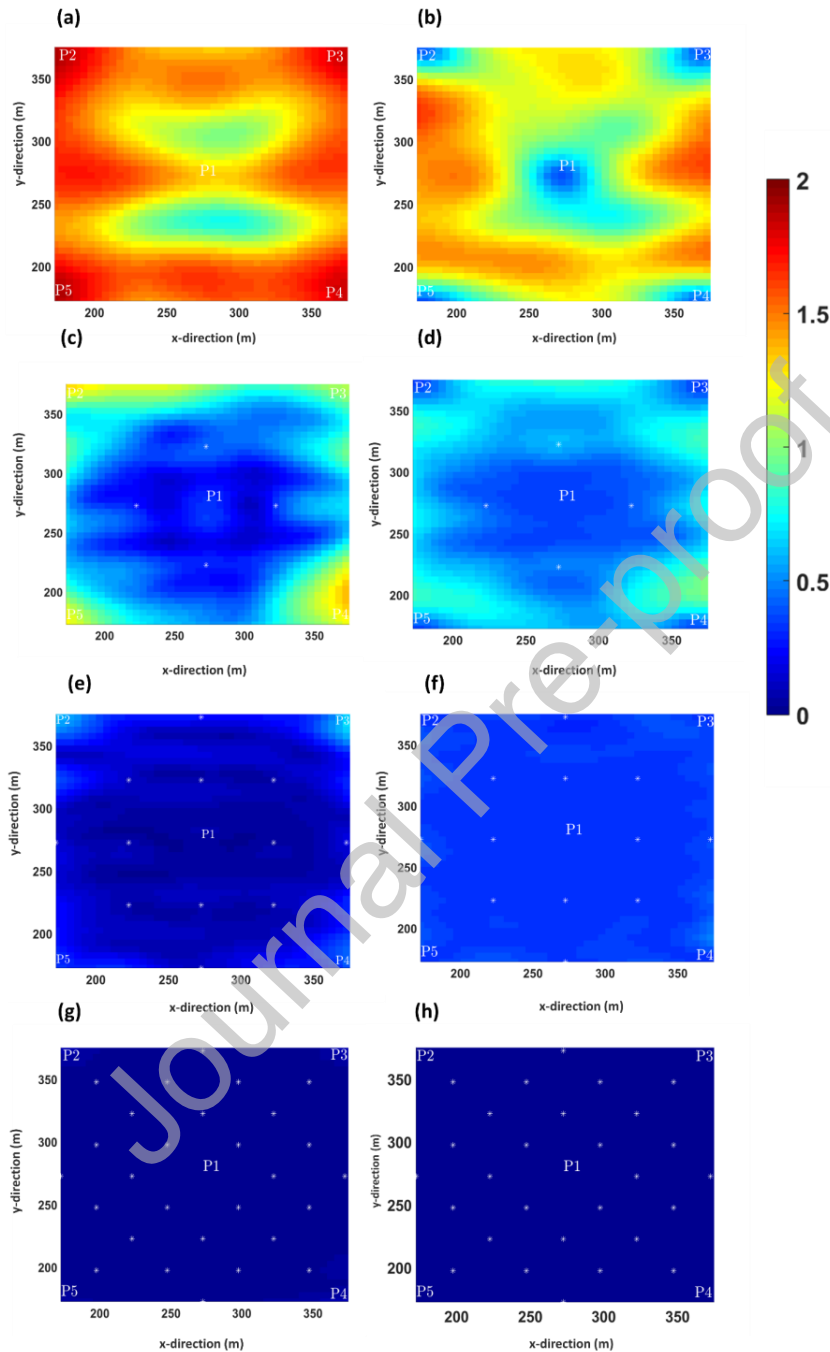
Variance	Boundary Condition	Number of observations	Frobenius norm	Correlation coefficient	Slope	Final WRMSE
4	Constant Rate	4	68.4	0.27	0.13	1.19
		8	48.27	0.75	0.62	1.05
		16	30.4	0.9	0.76	0.97
		32	23.47	0.94	0.95	1.1
		4	85.5	0.49	0.32	1.00
	Constant Head	8	75.15	0.68	0.48	0.96
		16	61.9	0.82	0.67	1.26
		32	54.90	0.9	0.93	1.23

358

359 For all cases, we find that changing the borehole boundary condition from constant rate to constant
 360 head deteriorates the Y-field estimation. This is quantified by the fact that the Frobenius norm (Table 1)
 361 increases from 68.4 to 85.5, 48.27 to 75.15, 30.4 to 61.9 and 23.47 to 54.90 for 4, 8, 16 and 32
 362 observation points, respectively. Comparing Figures 3(a) to 3(h) with the reference Y-field (Figure 3 (i))
 363 also show that cases with constant rate boundary conditions is visually closer to the reference Y-field.
 364 The use of constant head borehole boundary condition results in an underestimation of Y-field values
 365 and the mean value of Y-field. For instance, in the case of 4 observation points, the mean value of the
 366 estimated Y-field is around -4 for constant head boundary condition while it is -3.45 for constant rate
 367 boundary condition. The mean value of the reference Y-field is -3.57. Adding more observations leads to
 368 better results in terms of how close the estimated Y-field is to the reference Y-field as judged by the
 369 Frobenius norm, the correlation coefficient and the slope of the 1:1 line when estimated Y-field is to the
 370 reference Y-field are plotted against each other. This is reflected in the improvement of the correlation
 371 coefficient from 0.27 to 0.94 for constant rate borehole boundary condition and from 0.49 to 0.93 for
 372 constant head boundary condition when adding observation points. Associated increases in the slopes
 373 from 0.13 to 0.95 and from 0.32 to 0.93 for constant rate and constant head boundary conditions
 374 further underline the previous statement.

375 As expected, the standard deviations of the posterior covariance matrix (Figure 4) decrease as the
 376 number of observations increase. We also see that for the cases involving 8 (Figure 4(c)) and 16 (Figure
 377 4(e)) observation points with constant rate BC have lower uncertainties than the corresponding number

378 of observations (Figures 4(d) and 4(f)) with constant head BC. This is consistent with the previous
 379 statement of proper BC for head data.



380

381 **Figure 4:** Posterior standard deviation of estimated Y-field (variance 4) using hydraulic head data: **(a)** for
 382 4 observations point and constant rate B.C., **(b)** for 4 observations point and constant head B.C., **(c)** for 8
 383 observations point and constant rate B.C., **(d)** for 8 observations point and constant head B.C., **(e)** for 16

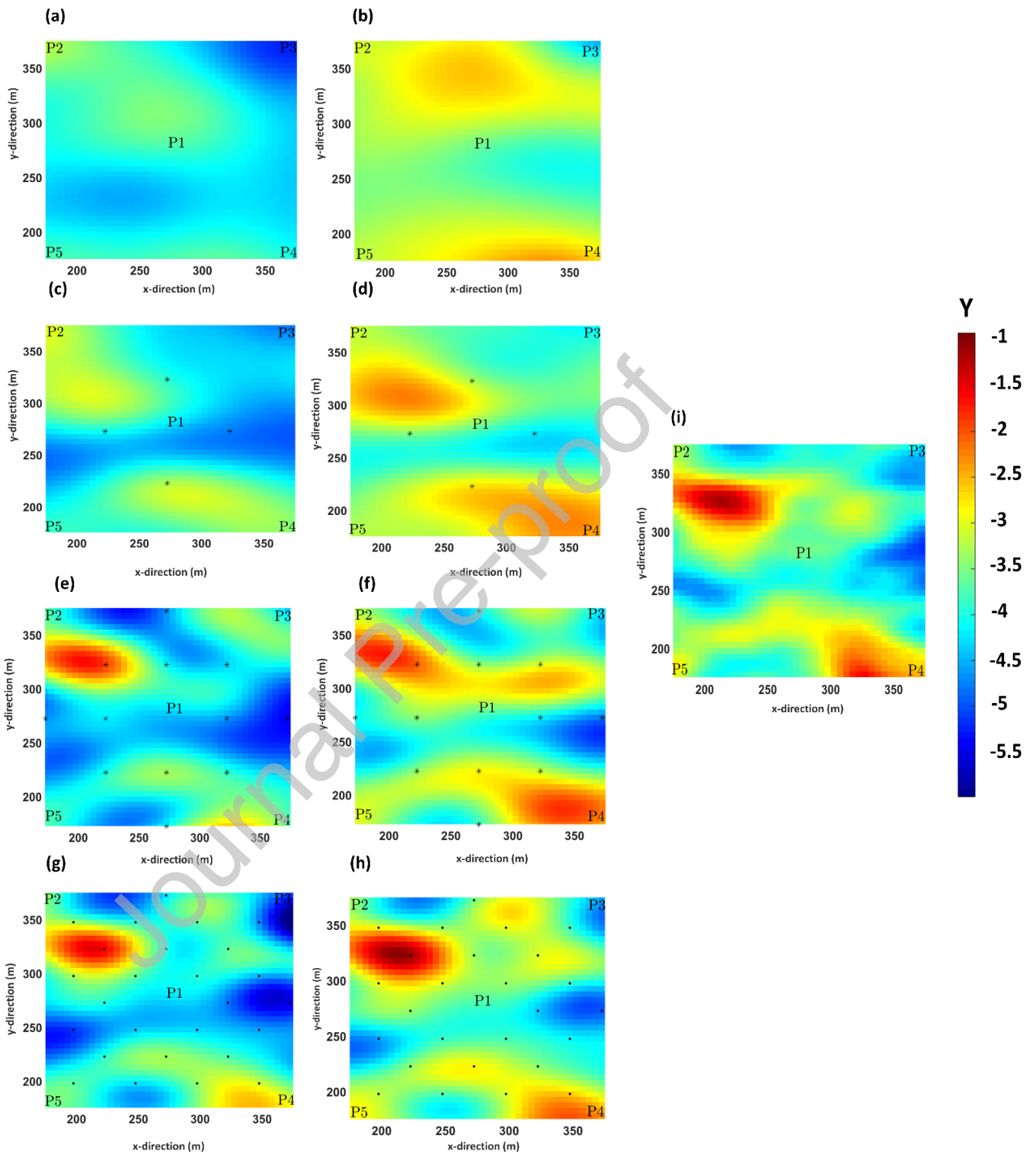
384 observations point and constant rate B.C., **(f)** for 16 observations point and constant head B.C., **(g)** for 32
385 observation points and constant rate B.C., **(h)** for 32 observation points and constant head B.C.

386

387 **4.2 Inversion of flux data**

388 We now consider the results obtained by individual inversions of flux data for a Y-field variance of 4.
389 Figure 5(a) to (h) show the Y-field estimates for 4, 8, 16 and 32 observation points subjected to constant
390 rate and constant head borehole boundary conditions. Table 2 provides the corresponding performance
391 metrics.

Journal Pre-proof



392
 393 **Figure 5:** Hydraulic conductivity field (variance 4) estimates from flux data: **(a)** inversion result for 4
 394 observations point and constant rate B.C., **(b)** inversion result for 4 observations point and constant
 395 head B.C., **(c)** inversion result for 8 observations point and constant rate B.C., **(d)** inversion result for 8

396 observations point and constant head B.C., **(e)** inversion result for 16 observations point and constant
 397 rate B.C., **(f)** inversion result for 16 observations point and constant head B.C., **(g)** inversion result for 32
 398 observation points and constant rate B.C., **(h)** inversion result for 32 observation points and constant
 399 head B.C., **(i)** reference Y -field

400 **Table 2:** Performance metrics (in the area of interest) from the inversion of flux data for the case of a Y -
 401 variance of 4.

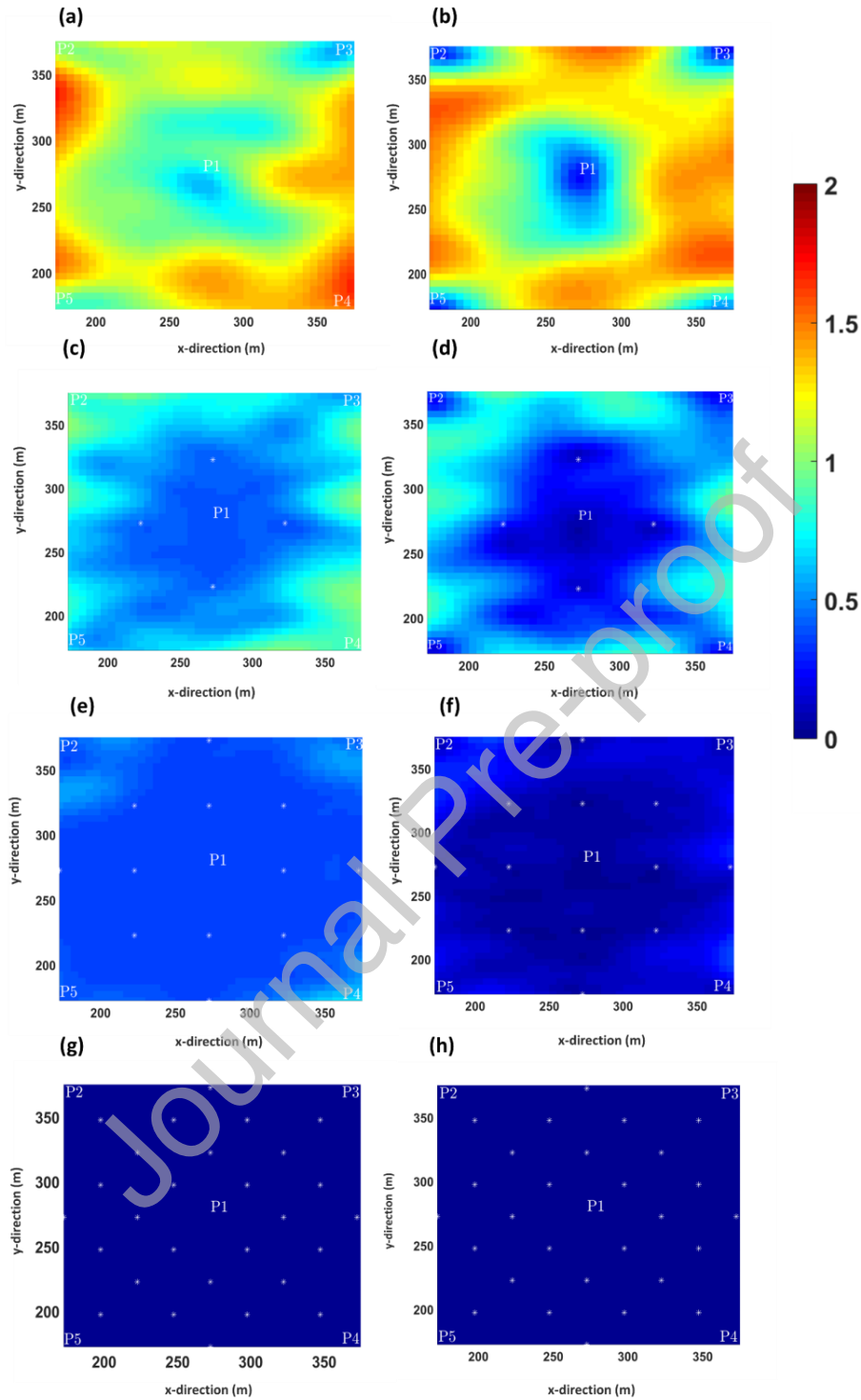
Variance	Boundary Condition	Number of observations	Frobenius norm	Correlation coefficient	Slope	Final WRMSE
4	Constant Rate	4	81.2	0.45	0.22	1.31
		8	65.61	0.76	0.56	1.19
		16	62.2	0.79	0.77	1.34
		32	53.6	0.9	0.90	2.12
	Constant Head	4	64.53	0.53	0.29	1
		8	47.7	0.77	0.61	1
		16	44.72	0.8	0.81	0.95
		32	32.03	0.92	0.91	1.45

402
 403 Contrary to head data, we find that constant head boundary conditions provide a better Y -field
 404 estimate when considering flux data. The better performance of the constant head (with respect to
 405 constant rate) boundary condition is seen, for instance, by comparing the values of the Frobenius norm
 406 given in Table 2. For the case of 4, 8, 16, and 32 observation points, the Frobenius norm decreases from
 407 81.2 to 64.53, 65.61 to 47.7, 62.2 to 44.7, and from 50.51 to 32.03, respectively. Using constant rate
 408 boundary condition for the flux data results in an underestimation of the Y -field mean. Considering the
 409 case with 4 observation points, the estimated Y -field's mean value with the constant rate boundary
 410 condition is around -4 while it is around -3.4 for the constant head boundary condition.

411
 412 Comparing the values of Frobenius norm for the head and flux data given in Table 1 and Table 2
 413 reveals that for a small number of observations (4 observation points), using flux data with constant
 414 head boundary condition gives a better Y -field estimate compared to head data with constant rate
 415 boundary condition as the Frobenius norm decreases from 68.4 to 64.53. This improvement is further
 416 supported by an increase in the correlation coefficient from 0.2744 to 0.446 and slope increase from
 417 0.127 to 0.22. For a larger number of observations, the performance of the two data types is similar
 418 when considering their ideal boundary conditions. It should be noted that inversion of head data using
 419 32 observation points (constant rate BC) results in an improved Y -field reconstruction when compared
 420 to inversion of the flux data with same number of observation (constant head BC). Despite the notable
 421 difference in Frobenius norm for this case, we can see the values of correlation coefficient and slope of

422 1:1 line is close to each other. Furthermore, final WRMSE for flux data is higher than head data (head
423 data are better converged than flux data) which may bring biasedness when comparing these two cases.
424 Finally, we do not observe the superiority of inversion of head data with 32 observation points (constant
425 rate BC) compared to inversion of flux data with 32 observations points (constant head BC) for hydraulic
426 conductivity field with lower variance.

427 The posterior standard deviation of the Y-field estimations is given in Figure 6. Again, the estimation
428 uncertainty decreases as the number of observations increase. Figure 6 (c) and (d) show the posterior
429 estimation uncertainty for 8 number of flux data observations using constant rate and constant head
430 BCs, respectively. It can be seen that using constant head BC results in lower uncertainty than constant
431 rate BC. Figures 6 (e) and 6 (f), which show posterior estimation uncertainty for 16 observation points of
432 flux data, when constant rate and constant head BCs are used, respectively. It can be seen that using
433 constant head BC for head data results in lower uncertainty of the estimated Y-field. This confirms our
434 previous statement about the proper BC for inversion of the flux data.



435
 436
 437 **Figure 6:** Posterior standard deviation of estimated Y-field (variance 4) using flux data: **(a)** for 4
 438 observations point and constant rate B.C., **(b)** for 4 observations point and constant head B.C., **(c)** for 8
 439 observations point and constant rate B.C., **(d)** for 8 observations point and constant head B.C., **(e)** for 16

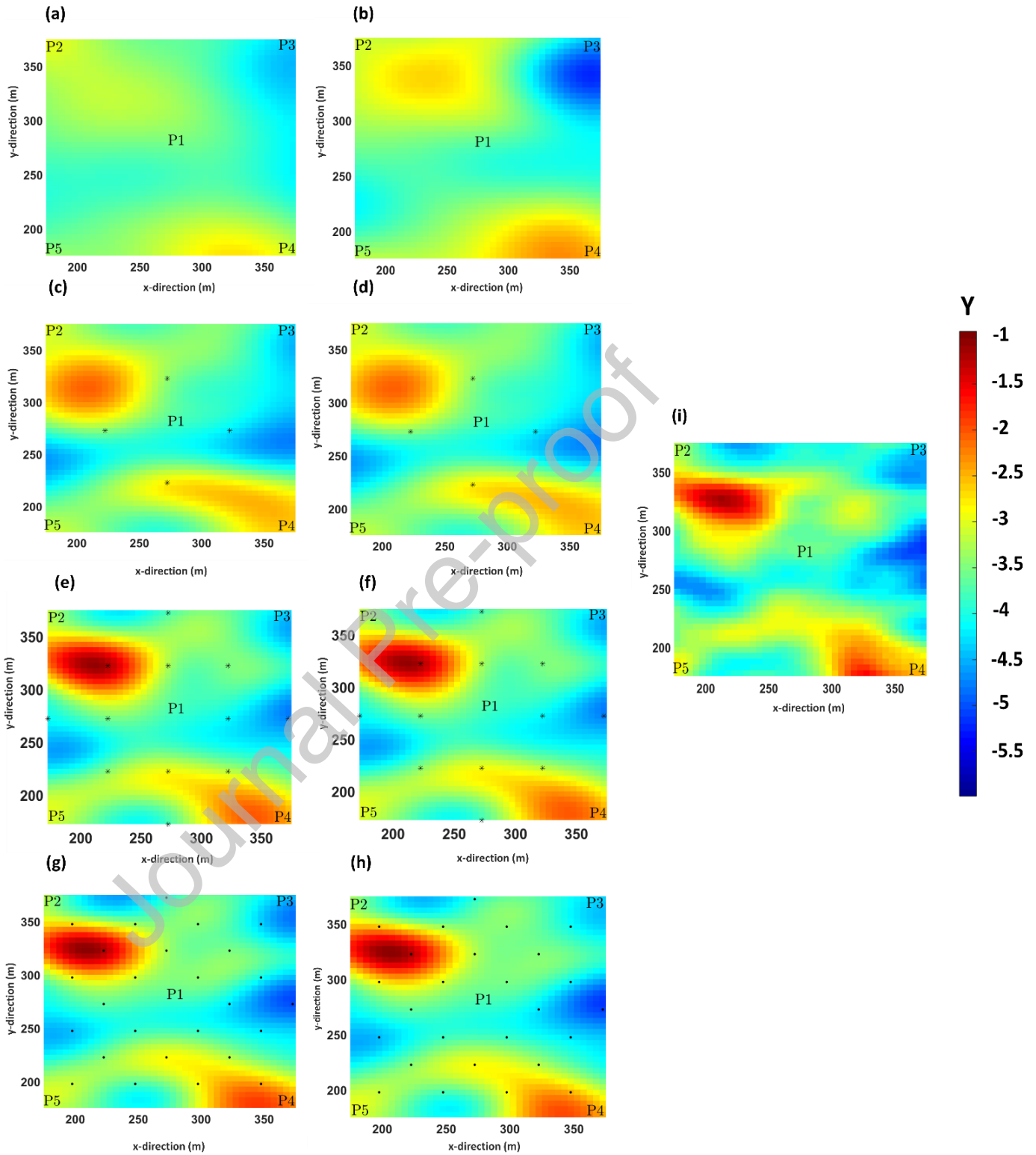
440 observations point and constant rate B.C., **(f)** for 16 observations point and constant head B.C., **(g)** for 32
441 observation points and constant rate B.C., **(h)** for 32 observation points and constant head B.C.

442

443 **4.3 Joint Inversion of flux and head data**

444 The results obtained by joint inversion of flux and head data are provided in Figure 7 (a) to (h) that
445 show the Y -field estimate for 8, 16, 32, and 64 observations subjected to the constant head and
446 constant rate borehole boundary conditions. The inversion metrics are outlined in Table 3. It should be
447 noted that we have two measurements (head and flux) for each point shown leading to 64 observations
448 for 32 observation points for instance.

Journal Pre-proof



449

450 **Figure 7:** Hydraulic conductivity field (variance 4) estimates from joint inversion: **(a)** inversion result for 4
 451 observations point and constant rate B.C., **(b)** inversion result for 4 observations point and constant

452 head B.C., **(c)** inversion result for 8 observations point and constant rate B.C., **(d)** inversion result for 8
 453 observations point and constant head B.C., **(e)** inversion result for 16 observations point and constant
 454 rate B.C., **(f)** inversion result for 16 observations point and constant head B.C., **(g)** inversion result for 32
 455 observation points and constant rate B.C., **(h)** inversion result for 32 observation points and constant
 456 head B.C., **(i)** reference Y-field

457 **Table 3:** Performance metrics for joint inversion of head and flux data in the area of interest

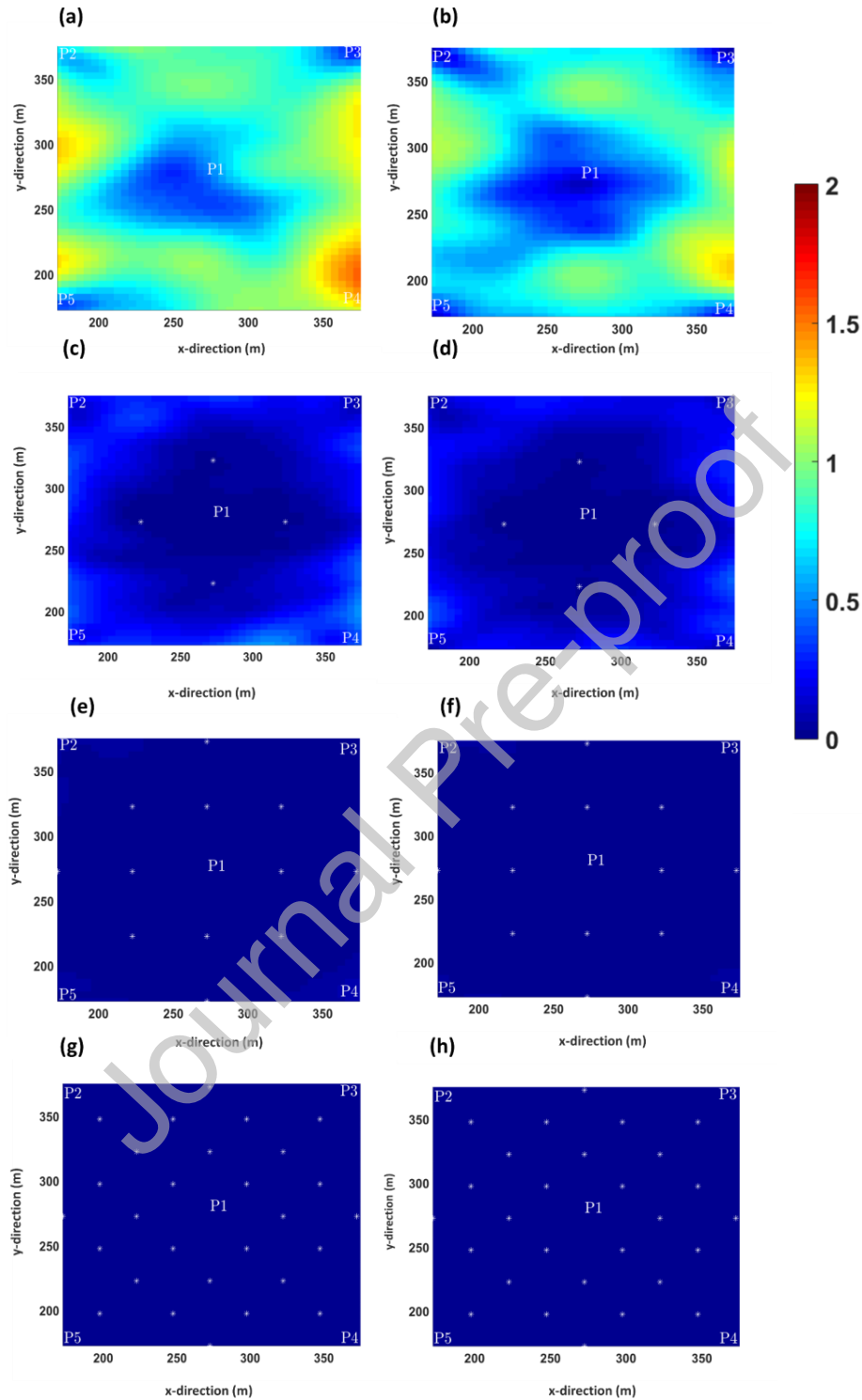
Variance	Boundary Condition	Number of observations	Frobenius norm	Correlation coefficient	Slope	Final WRMSE
4	Constant Rate	8	51.8	0.7	0.34	0.8
		16	39.7	0.82	0.68	1.24
		32	24.44	0.94	0.92	2.25
		64	22	0.96	0.98	1.13
	Constant Head	8	53.97	0.64	0.51	1.1
		16	38.34	0.84	0.74	1.13
		32	27.38	0.93	0.92	1.5
		64	21.71	0.95	0.97	1.65

458
 459 The Frobenius norms for 8, 16, 32 and 64 observations are 51.8, 39.7, 24.44 and 22, respectively,
 460 when considering constant head borehole boundary conditions, while they are 53.97, 38.34, 27.38 and
 461 21.71 for constant rate boundary condition. For the same number of observations, the Frobenius norms
 462 are very similar regardless of borehole boundary conditions. In contrast to individual inversions, this
 463 suggests that they do not significantly affect the results obtained by joint inversion.

464 The joint inversion results (Table 3) do not demonstrate any significant improvement compared to
 465 the individual inversions (Tables 1 and 2) when considering the same number of observations. For 8
 466 observations, the minimum Frobenius norm obtained for head, flux and joint inversion are 48.27, 47.7
 467 and 51.8, respectively. For 16 observations, the minimum Frobenius norm obtained for head, flux and
 468 joint inversion are 30.4, 44.72 and 38.34, respectively while it is 23.47, 32.03 and 24.44 for 32
 469 observations. When considering the same number of observation points, the joint inversion has twice as
 470 many observations as the individual inversions. This leads to significantly better estimates of the
 471 hydraulic conductivity field.

472 Figure 8 shows the posterior estimation uncertainty of joint inversion of flux and head data for
 473 different number of observations and different type of BCs. Comparing the cases with same number of
 474 observations (different borehole BCs), we do not observe any notable difference in estimation
 475 uncertainty depending on BC. This is also consistent with our previous statement regarding the fact that
 476 borehole BCs play no significant role in joint inversion of head and flux data.

477



478
 479 **Figure 8:** Posterior Standard deviation of estimated Y-field (variance 4) using both head and flux data: (a)
 480 for 4 observations point and constant rate B.C., (b) for 4 observations point and constant head B.C., (c)
 481 for 8 observations point and constant rate B.C., (d) for 8 observations point and constant head B.C., (e)

482 for 16 observations point and constant rate B.C., **(f)** for 16 observations point and constant head B.C., **(g)**
483 for 32 observation points and constant rate B.C., **(h)** for 32 observation points and constant head B.C.

484

485 **5. DISCUSSION**

486 **5.1 General findings**

487 Considering the results of all 96 inversion scenarios considered, we find that inversion of flux data
488 (with appropriate borehole boundary condition) leads to better resolved Y -field estimates than when
489 considering head data particularly when a small number of observations are available. Furthermore, the
490 quality of the inversion results is strongly dependent on the type of boundary condition used in the
491 borehole. The performance metrics in Tables 1 and 2 suggest that it is more suitable to use constant rate
492 borehole boundary condition for head data and constant head borehole boundary condition for the flux
493 data as reflected in Frobenius norms' values. The reason is that if the observation is head data and the
494 borehole boundary is set to constant head, the model response (head) will have less sensitivity to
495 change of Y -field values. The same argument is also valid for the flux data. Once pumping with a
496 constant rate, the value of groundwater flux is fixed, and the distribution of hydraulic gradient will be
497 dependent on the distribution of the hydraulic conductivity. This means that measured groundwater
498 flux would not be so sensitive to the distribution of hydraulic conductivity. When pumping with a
499 constant head, the head gradient would be fixed, and the distribution of the groundwater flux will be
500 highly dependent on the distribution of the hydraulic conductivity while the hydraulic gradient would
501 not be very dependent on the distribution of the hydraulic conductivity. Even though no specific
502 sensitivity analysis was performed but the explained behavior could be seen in the calculated Jacobian
503 matrix values (the sensitivity of the forward model output at observation points with respect to the
504 unknown model parameters) which were quite much smaller in case of inappropriate boundary
505 conditions. The estimation uncertainty for head, flux and joint inversion of both data reveals the role of
506 boundary condition in the reconstruction of the Y -field. Inversion of head data with constant rate BC
507 results in lower uncertainty than using constant head BC. Inversion of the flux data using constant head
508 BC will be less uncertain than using constant rate BC. However, the estimation uncertainty for joint
509 inversion of both data is almost the same for both type of BCs. Further studies, which consider transient
510 hydraulic tomography and 3D porous media, would be very useful to confirm and investigate how
511 quality of the inversion results depends on the type of boundary condition.

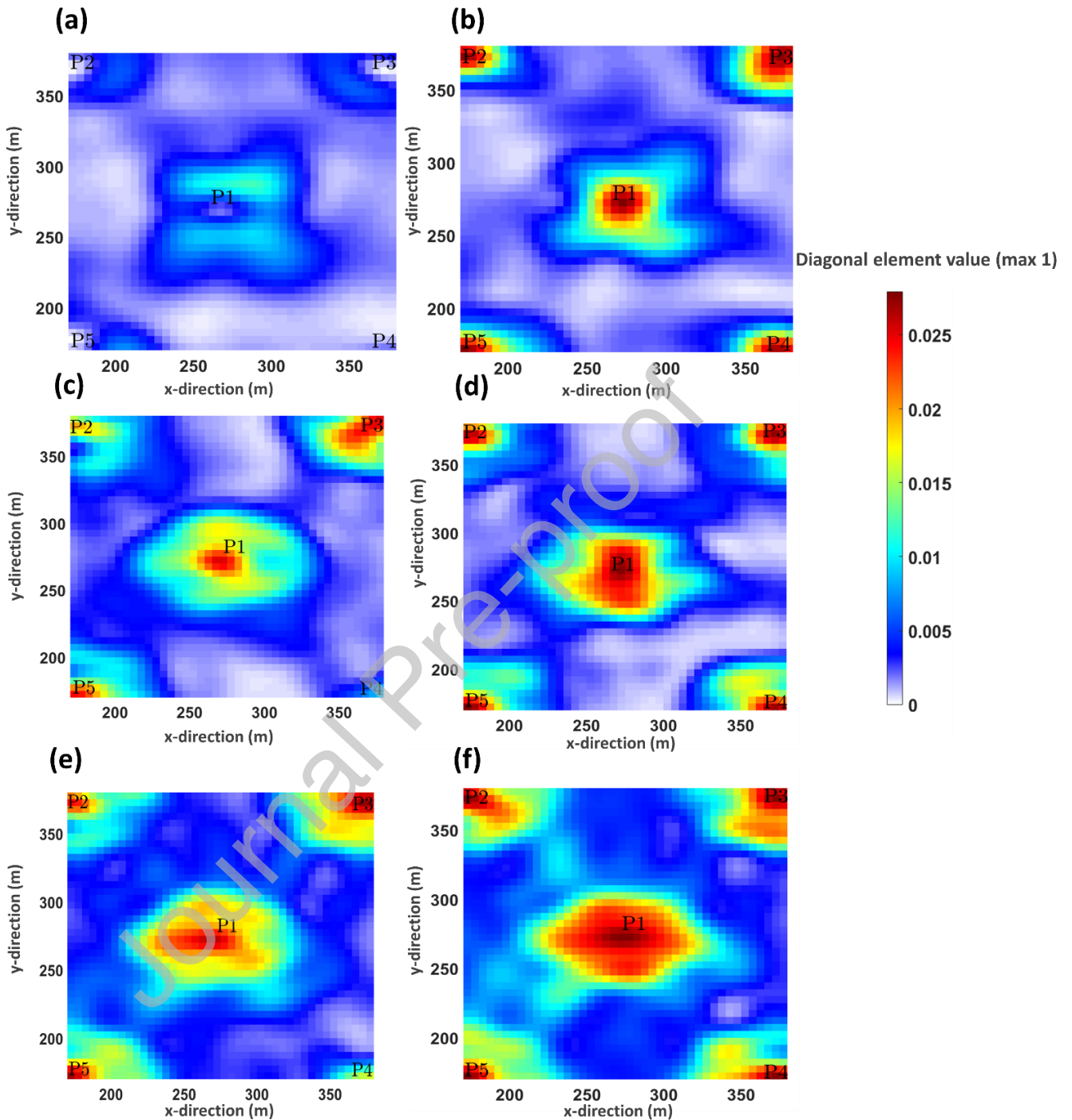
512

513 This may indeed have some consequences for field experiment where the effect of the borehole
514 boundary is essential for proper experimental design. Our results suggest that the experimental designs
515 should ensure that once head data are intended to be used for the inversion, wells must be pumped at a
516 constant rate while for the inversion of the flux data, the head in the borehole should be kept fixed.
517 Other borehole boundary conditions lead to an underestimation of hydraulic conductivity values.
518 However, for the joint inversion of both data, the type of borehole boundary conditions does not play a
519 significant role.

520

521 Tso et al. (2016) and Zha et al. (2014) found that joint inversion of head and flux data results in
522 better estimation of Y -fields in porous and fractured media compared to the head data. Here, we find
523 that joint inversion does not offer any advantage over the individual inversion of the flux and head data
524 when considering an equal number of observations and ideal borehole boundary conditions. However,
525 measurements distributed across the aquifer could potentially reveal more information about the
526 heterogeneity. Our results rather suggest that, for a constant signal-to-noise-ratio, the inversion
527 performance depends largely on the number of observations. For a small number of observations, the
528 flux data provides a superior Y -field estimate compared to inversion of head data, while for the higher
529 number of observations, all data types perform similarly. However, if we would be able to measure flux
530 and head data at the same location, then for the same number of observation points, joint inversion of
531 flux and head data provide better estimates of Y -field as the number of observations are doubled.
532 Furthermore, we demonstrated the importance of borehole boundary conditions for hydraulic
533 tomography experimental design when performing individual inversions.

534
535 A resolution analysis for the case of the variance of 4 and 4 measurement points demonstrates that
536 flux data can better resolve the hydraulic conductivity field compared to head data (Figure 9). Figure 9
537 shows the diagonal elements of the resolution matrix (calculated in the final inversion iteration) for
538 head data, flux data, and joint inversion of both data are plotted on their corresponding blocks,
539 respectively. Considering the best Y -field estimates obtained for the head (constant rate boundary
540 condition) and flux (constant head boundary condition) data for calculating the resolution matrices, as
541 shown in Figure 9 (a) and 9 (d), it can be stated that model parameters (hydraulic conductivity values)
542 are better resolved by flux data. This is manifested by comparing both the values and coverage area of
543 diagonal elements larger than 0.005. When head data are used for the inversion, the degree of
544 smoothing and averaging is higher compared to the case in which the flux data are used. It is worth
545 noting that, since PCGA does not calculate the full Jacobian matrix, it has the potential to blur the
546 resolution matrix. However, we have chosen more PCA elements than recommended to ensure high
547 fidelity realizations with respect to original geostatistical model



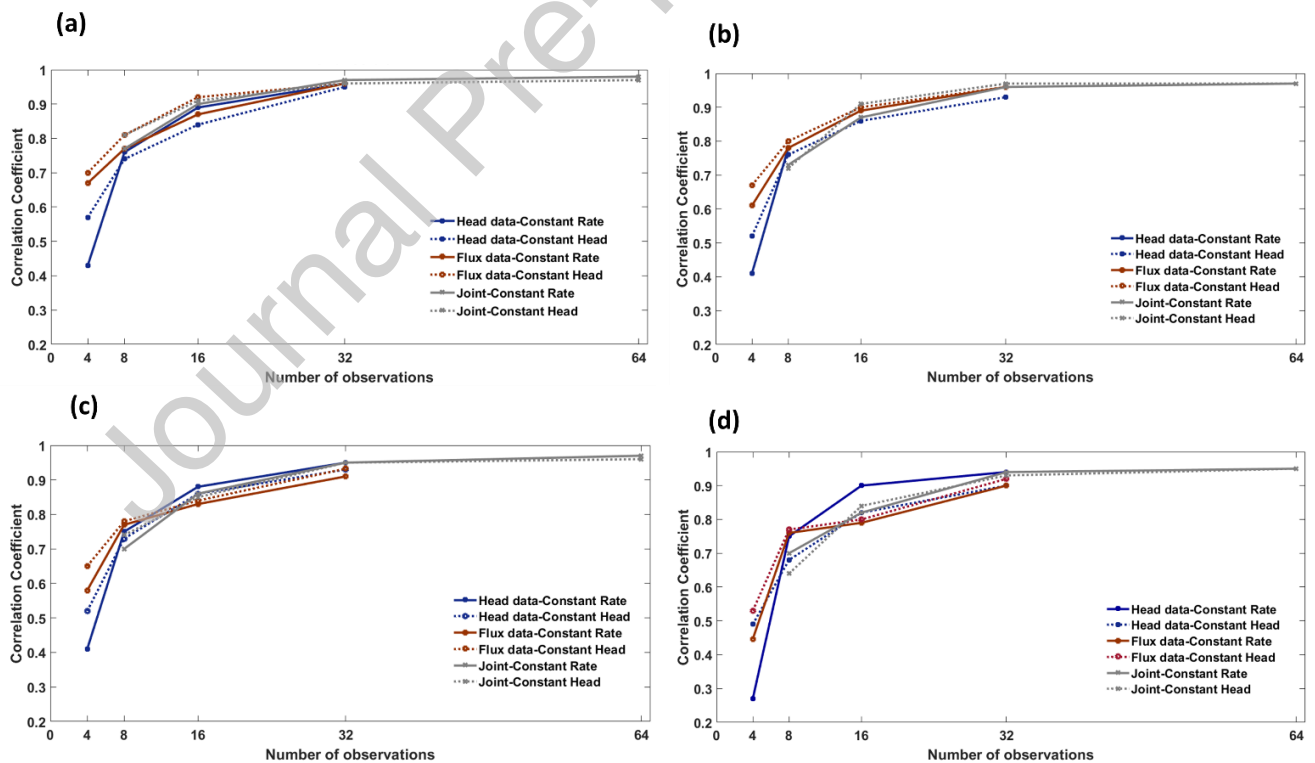
548
 549 **Figure 9:** Diagonal element of the resolution matrix for (a) Y-field obtained by inversion of head data (4
 550 observation points - borehole boundary is set to constant rate), (b) Y-field obtained by inversion of head
 551 data (4 observation points - borehole boundary is set to constant head), (c) Y-field obtained by inversion
 552 of flux data (4 observation points - borehole boundary is set to constant head), (d) Y-field obtained by
 553 inversion of flux data (4 observation points - borehole boundary is set to constant rate), (e) Y-field
 554 obtained by joint inversion of both data (4 observation points - borehole boundary is set to constant

555 rate), (f) Y -field obtained by joint inversion of both data (4 observation points - borehole boundary is set
556 to constant head).

557 5.2 The effect of number of observations and variance

558 Figures 10 (a) to (d) show the correlation coefficient (between estimated Y -field and reference Y -
559 field) versus the number of observations for different type of data and borehole boundary conditions. It
560 is seen that as the number of observations increases, the correlation coefficient also increases for all
561 types of data and boundary conditions. For a small number of observations, flux data are superior to
562 head data. The difference between the correlation coefficient of flux and head data is the strongest for a
563 small number of observations, while the difference gradually decreases as the number of observations
564 increases and at a high number of observations, they converge. This is a consequence of the decreasing
565 distance between data points as the number of observations increases, thereby decreasing the radius of
566 averaging. The gains by joint inversion for a prescribed number of observation points is that
567 performance is independent of the borehole boundary condition and we need half as many boreholes if
568 we are able to measure head and flux data at the same location.

570 The variance of the hydraulic conductivity field affects the final values of the correlation coefficient.
571 The higher the variance, the lower the correlation coefficient (especially for a small number of
572 observations), and also the more challenging it is to reach a WRMSE close to 1.



573
574 **Figure 10:** Correlation coefficient versus number of observations for reference hydraulic conductivity
575 field with (a) variance=0.5, (b) variance=1 (c), variance=2 (d), variance=4. The Blue, red and gray color
576 show the results for head data, flux data and joint inversion of both data, respectively. The data with

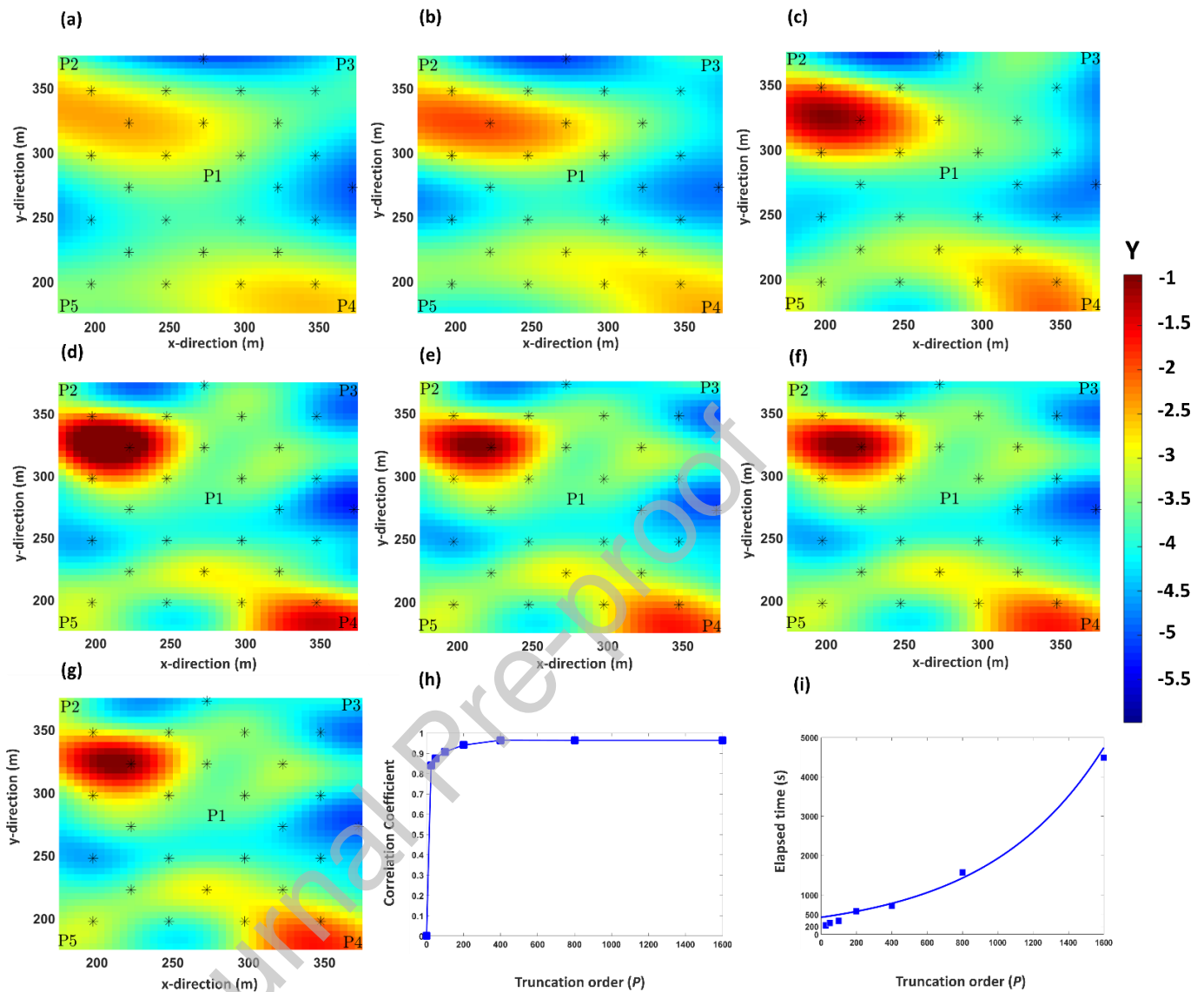
577 constant rate borehole boundary condition is marked with solid line while the data with constant head
578 borehole boundary condition is shown by the dashed line.

579

580 **5.3 The effect of truncation order (P) on final inversion results**

581 One of the inversion cases (variance of 4, 32 observation points, joint inversion of head and flux
582 data) was chosen to investigate the effect of the truncation order (P) on the final inversion result.
583 Inversions were performed using truncation orders of 25, 50, 100, 200, 400, 800, and 1600. The
584 inversions were performed on a server with one Terabyte (1 Tb) memory, 4 processors (Intel Xeon CPU
585 E7-4850 v4 @ 2.10 GHz) and 40 cores in parallel mode. Figure 11 shows the Y -field estimated for each P
586 value, the effect on the correlation coefficient, and elapsed time for each geostatistical iteration. For a
587 truncation order of 25, we capture an overly smooth version of the true model with a correlation
588 coefficient of 0.84. By setting the truncation order to 50, 100, and 200, the correlation coefficient
589 increases to 0.88, 0.91, and 0.94, respectively. The truncation order of 400 (used in our study) with a
590 correlation coefficient of 0.96 is the point beyond which increasing the truncation order does not
591 significantly improve the correlation coefficient. So, the truncation order leads to improvement of Y -
592 field reconstruction up to some points and after this point, it is only the computational time that
593 increases as the inversion performance is data limited. The computational time increased exponentially
594 for large P values. The right choice of P is critical to ensure sufficient reconstruction of the hydraulic
595 conductivity field while keeping the computational time low. The truncation order should be chosen
596 based on the degree of heterogeneity and the computational resource available. It would help perform
597 inversion using different numbers of principal components to ensure the proper choice of the number of
598 principal components.

599



600
 601 **Figure 11:** Estimated Y-field for truncation order of (a) 25, (b) 50, (c) 100, (d) 200, (e) 400, (f) 800, (g)
 602 1600. (h) Correlation coefficient versus truncation order, (i) elapsed time per one iteration versus
 603 truncation order

604

605 5.4 Implications for field implementations

606 Our results highlight the added value of using the flux data individually or jointly with head data in
 607 hydraulic tomography to achieve an enhanced reconstruction of the hydraulic conductivity field
 608 compared to using head data alone. This improvement is particularly pronounced when considering a
 609 small number of observations, a more likely setting for field applications. However, using only flux data
 610 requires setting the borehole boundary condition to constant head, which is feasible (using pumps
 611 whose rates are controlled with water level) but would be more challenging than pumping at a constant

612 rate during the field experiments. However, measuring the flux data during pumping (with constant
613 rate) and joint inversion of both data would be quite feasible and removes the limitation of the borehole
614 boundary condition. Additional simulations (not shown) revealed that adding even one relevant
615 observation (head data once pumping with constant rate and flux data once pumping with constant
616 head) allowed for proper estimation of the hydraulic conductivity. Moreover, if one could measure the
617 head and flux data at the same location, by doubling the number of observations, the Y -field estimate
618 would be significantly improved. The potential application of FO cables for pressure measurement is
619 discussed by Butler et al. (1999) and a recent application for drawdown measurements during pumping
620 tests is demonstrated by Tiedeman and Barrash (2020). A proper setting for the collection of head and
621 flux data could include head measurements at boreholes while taking flux measurements at other
622 locations using the FO-DTS technique. It is also worth noting that groundwater flux measurement is not
623 as easy as measuring the head since it requires much more equipment than a simple pressure sensor. It
624 is also true that one can measure the water level in all environments while groundwater flux
625 measurement is currently possible for granular, unconsolidated aquifers (Simon et al., 2021). On the
626 other hand, FO-DTS measurements may provide groundwater flux data at a high spatial resolution
627 (Simon et al., 2020).

628 The results presented in this paper are only valid for steady-state hydraulic tomography. The
629 method for measuring groundwater flux from active FO-DTS experiments estimates has been developed
630 works in steady-state hydraulic conditions (des Tombes et al., 2019; Simon et al., 2021, del Val et al,
631 2021), so we used steady state also for head data. Transient hydraulic tomography would probably
632 result in better reconstruction of hydraulic conductivity field estimation. Transient hydraulic
633 tomography provides the opportunity to resolve the storage, thanks to the numerous transient data
634 available. The best practice would be to use all available information (transient hydraulic head data) and
635 use groundwater flux data as additional constraint.

636 6. CONCLUSIONS

637 We used a numerical model representing a one-layer heterogeneous aquifer along with a
638 geostatistical inversion approach (PCGA) to assess the information content of head and flux data. We
639 varied the observation type, the number of observation points, the hydraulic conductivity variance (with
640 the same field structure) and the borehole boundary conditions. For a small number of observation
641 points, we find that flux data produced a better Y -field compared to head data. When increasing the
642 number of observation points and using appropriate borehole boundary conditions, the effect of the
643 data type vanishes, and all converge to the same results as the sampling distance between points
644 becomes smaller. For the same number of observation points, if we are able to measure the head and
645 flux data at the same location, joint inversion of head and flux data provides an improved estimate
646 compared to the individual inversion of head or flux data due to the doubling of the number of
647 observations. This means that the head and flux data measured at the same location provide
648 complementary information. The type of borehole boundary conditions used in the tomography and
649 modeling affects the inversion results. The appropriate boundary condition for head and flux data is
650 constant rate and constant head, respectively, while joint inversion performance is independent of the

651 boundary type. Inappropriate selection of borehole boundary conditions may result in an
652 underestimation of the Y -field values which is also reflected in posterior estimation uncertainties.
653 Comparing the estimation uncertainty, it can be seen that using head and flux data with inappropriate
654 borehole BC results in higher uncertainty compared to the case when proper borehole BCs are used.
655 Measuring flux data during a hydraulic tomography experiment is now feasible, especially for shallow
656 sandy aquifers where active Distributed Temperature Sensing, can be deployed using direct push
657 method to install the fiber optic cables into the sediments. Since the inversion is particularly sensitive to
658 the number of measurements, groundwater flux measurements by active DTS can be particularly useful
659 since it may provide a large number of measurements thanks to the high spatial resolution of fiber optic
660 temperature measurements. Moreover, it can be also particularly useful in aquifers where the head
661 drop due to the pumping is small, but there may be high groundwater fluxes. This should lead to
662 interesting developments of hydraulic tomography experiments in the near future.

663 7. ACKNOWLEDGMENTS

664 ENIGMA ITN project that has received funding from the European Union's Horizon 2020 research
665 and innovation programme under the Marie Skłodowska-Curie Grant Agreement No 722028. In our
666 work we relied on the PCGA implementation in Python (pyPCGA) by Lee et al. (2016) available on GitHub
667 (<https://github.com/jonghyunharrylee/pyPCGA/>). We would like to appreciate SINTEF for providing free
668 access to the Matlab Reservoir Simulator Tool (MRST) which is available on the SINTEF website
669 (<https://www.sintef.no/projectweb/mrst/>). We would like to thank Dr. Ty Ferre and two anonymous
670 reviewers for the comments that greatly helped us improve the manuscript.

671 CRediT authorship statement

672 **Behzad Pouladi:** Writing - original draft, Writing - review & editing, Methodology, Conceptualization,
673 Software, Formal analysis, Investigation. **Niklas Linde:** Conceptualization, Methodology, Supervision,
674 Writing, Supervision, Writing - original draft, Writing - review & editing. **Laurent**
675 **Longuevergne:** Supervision. **Olivier Bour:** Writing - review & editing, Conceptualization, Writing - review
676 & editing.

677 DECLARATION OF COMPETING INTEREST

678 The authors declare that they have no known competing financial interests or personal relationships
679 that could have influenced the work reported in this paper.

680

681

682 **REFERENCES**

- 683 Alumbaugh, D.L., Newman, G.A., 2000. Image appraisal for 2-D and 3-D electromagnetic inversion.
684 *Geophysics* 65, 1455–1467.
- 685 Bakker, M., Caljé, R., Schaars, F., van der Made, K., de Haas, S., 2015. An active heat tracer experiment
686 to determine groundwater velocities using fiber optic cables installed with direct push equipment.
687 *Water Resour. Res.* 51, 2760–2772.
- 688 Ballard, S., G.T. Barker, R.L. Nichols, 1996, A test of the in situ permeable flow sensor at Savannah River,
689 South Carolina, *Groundwater*, volume 34, number 3, pages 389-396.
- 690 Berg, S.J., Illman, W.A., 2015. Comparison of hydraulic tomography with traditional methods at a highly
691 heterogeneous site. *Groundwater* 53, 71–89.
- 692 Berg, S.J., Illman, W.A., 2013. Field study of subsurface heterogeneity with steady-state hydraulic
693 tomography. *Groundwater* 51, 29–40.
- 694 Berg, S.J., Illman, W.A., 2011. Three-dimensional transient hydraulic tomography in a highly
695 heterogeneous glaciofluvial aquifer-aquitard system. *Water Resour. Res.* 47(10).
- 696 Bohling, G.C., Butler Jr, J.J., 2010. Inherent limitations of hydraulic tomography. *Groundwater* 48, 809–
697 824.
- 698 Bohling, G.C., Butler Jr, J.J., Zhan, X., Knoll, M.D., 2007. A field assessment of the value of steady state
699 hydraulic tomography for characterization of aquifer heterogeneities. *Water Resour. Res.* 43, 60–
700 61.
- 701 Brauchler, R., Hu, R., Dietrich, P., Sauter, M., 2011. A field assessment of high-resolution aquifer
702 characterization based on hydraulic travel time and hydraulic attenuation tomography. *Water*
703 *Resour. Res.* 47(3).
- 704 Brauchler, R., Hu, R., Hu, L., Jiménez, S., Bayer, P., Dietrich, P., Ptak, T., 2013. Rapid field application of
705 hydraulic tomography for resolving aquifer heterogeneity in unconsolidated sediments. *Water*
706 *Resour. Res.* 49, 2013–2024.
- 707 Brauchler, R., Hu, R., Vogt, T., Al-Halbouni, D., Heinrichs, T., Ptak, T., Sauter, M., 2010. Cross-well slug

- 708 interference tests: An effective characterization method for resolving aquifer heterogeneity. J.
709 Hydrol. 384, 33–45.
- 710 Brauchler, R., Liedl, R., Dietrich, P., 2003. A travel time based hydraulic tomographic approach. Water
711 Resour. Res. 39(12).
- 712 Butler Jr, J.J., McElwee, C.D., Bohling, G.C., 1999. Pumping tests in networks of multilevel sampling wells:
713 Motivation and methodology. Water Resour. Res. 35, 3553–3560.
- 714 Cardiff, M., Bakhos, T., Kitanidis, P.K., Barrash, W., 2013. Aquifer heterogeneity characterization with
715 oscillatory pumping: Sensitivity analysis and imaging potential. Water Resour. Res. 49, 5395–5410.
- 716 Cardiff, M., Barrash, W., 2011. 3-D transient hydraulic tomography in unconfined aquifers with fast
717 drainage response groundwater flow parameters (primarily , hydraulic conductivity K) in
718 permeable , unconfined aquifers . To invert the large amount of transient data collected from 3DT
719 47(12). <https://doi.org/10.1029/2010WR010367>
- 720 Cardiff, M., Barrash, W., Kitanidis, P.K., Malama, B., Revil, A., Straface, S., Rizzo, E., 2009. A potential-
721 based inversion of unconfined steady-state hydraulic tomography. Groundwater 47, 259–270.
- 722 Day-Lewis, F.D., Singha, K., Binley, A.M., 2005. Applying petrophysical models to radar travel time and
723 electrical resistivity tomograms: Resolution-dependent limitations. J. Geophys. Res. Solid Earth
724 110(8). 1-17.
- 725 del Val, L., Carrera, J., Pool, M., Martinez, L., Casanovas, C., Bour, O., & Folch, A. (2021). Heat dissipation
726 test with fiber-optic distributed temperature sensing to estimate groundwater flux. Water
727 Resources Research, 57, e2020WR027228. <https://doi.org/10.1029/2020WR027228>
- 728 Devlin, J.F., 2020, [Groundwater Velocity](#). The Groundwater Project, Guelph, Ontario, Canada.
- 729 des Tombe, B.F., Bakker, M., Smits, F., Schaars, F., van der Made, K., 2019. Estimation of the variation in
730 specific discharge over large depth using distributed temperature sensing (DTS) measurements of
731 the heat pulse response. Water Resour. Res. 55, 811–826.
- 732 Doro, K.O., Cirpka, O.A., Leven, C., 2015. Tracer tomography: Design concepts and field experiments
733 using heat as a tracer. Groundwater 53, 139–148.
- 734 Drost, W., Klotz, D., Koch, A., Moser, H., Neumaier, F., Rauert, W., 1968. Point dilution methods of

- 735 investigating ground water flow by means of radioisotopes. *Water Resour. Res.* 4, 125–146.
- 736 Fakhreddine, S., Lee, J., Kitanidis, P.K., Fendorf, S., Rolle, M., 2016. Imaging geochemical heterogeneities
737 using inverse reactive transport modeling: An example relevant for characterizing arsenic
738 mobilization and distribution. *Adv. Water Resour.* 88, 186–197.
- 739 Fiene, M.N., Clemons, T., Kitanidis, P.K., 2008. An interactive Bayesian geostatistical inverse protocol for
740 hydraulic tomography. *Water Resour. Res.* 44(12).
- 741 Fischer, P., Jardani, A., Soueid Ahmed, A., Abbas, M., Wang, X., Jourde, H., Lecoq, N., 2017. Application
742 of Large-Scale Inversion Algorithms to Hydraulic Tomography in an Alluvial Aquifer. *Groundwater*
743 55, 208–218.
- 744 Gottlieb, J., Dietrich, P., 1995. Identification of the permeability distribution in soil by hydraulic
745 tomography. *Inverse Probl.* 11, 353-360.
- 746 Huang, S., Wen, J., Yeh, T.J., Lu, W., Juan, H., Tseng, C., Lee, J., Chang, K., 2011. Robustness of joint
747 interpretation of sequential pumping tests: Numerical and field experiments. *Water Resour. Res.*
748 47(10).
- 749 Illman, W. a, Liu, X., Craig, A., 2008. Evaluation of transient hydraulic tomography and common hydraulic
750 characterization approaches through laboratory sandbox experiments. *J. Environ. Eng. Manag.* 18,
751 249–256.
- 752 Illman, W.A., Berg, S.J., Zhao, Z., 2015. Should hydraulic tomography data be interpreted using
753 geostatistical inverse modeling? A laboratory sandbox investigation. *Water Resour. Res.* 51, 3219–
754 3237.
- 755 Illman, W.A., Zhu, J., Craig, A.J., Yin, D., 2010. Comparison of aquifer characterization approaches
756 through steady state groundwater model validation: A controlled laboratory sandbox study. *Water*
757 *Resour. Res.* 46(4).
- 758 Jamin, P., Goderniaux, P., Bour, O., Le Borgne, T., Englert, A., Longuevergne, L., Brouyère, S., 2015.
759 Contribution of the finite volume point dilution method for measurement of groundwater fluxes in
760 a fractured aquifer. *J. Contam. Hydrol.* 182, 244–255.
- 761 Jim Yeh, T., 1992. Stochastic modelling of groundwater flow and solute transport in aquifers. *Hydrol.*

- 762 Process. 6, 369–395.
- 763 Jiménez, S., 2015. High resolution aquifer characterization using hydraulic tomography and tracer
764 tomography. PhD diss., ETH Zurich, 2015.
- 765 Jiménez, S., Mariethoz, G., Brauchler, R., Bayer, P., 2016. Smart pilot points using reversible-jump
766 Markov-chain Monte Carlo. *Water Resour. Res.* 52, 3966–3983.
- 767 Kang, P.K., Lee, J., Fu, X., Lee, S., Kitanidis, P.K., Juanes, R., 2017. Improved characterization of
768 heterogeneous permeability in saline aquifers from transient pressure data during freshwater
769 injection. *Water Resour. Res.* 53, 4444–4458.
- 770 Kearl, P.M., 1997. Observations of particle movement in a monitoring well using the colloidal borescope.
771 *J. Hydrol.* 200, 323–344.
- 772 Klepikova, M. V, Le Borgne, T., Bour, O., de Dreuzy, J., 2013. Inverse modeling of flow tomography
773 experiments in fractured media. *Water Resour. Res.* 49, 7255–7265.
- 774 Kowalsky, M.B., Finsterle, S., Rubin, Y., 2004. Estimating flow parameter distributions using ground-
775 penetrating radar and hydrological measurements during transient flow in the vadose zone. *Adv.*
776 *Water Resour.* 27, 583–599.
- 777 Kuhlman, K.L., Hinnell, A.C., Mishra, P.K., Yeh, T.J., 2008. Basin-scale transmissivity and storativity
778 estimation using hydraulic tomography. *Groundwater* 46, 706–715.
- 779 Labaky, W., J.F. Devlin, R.W. Gillham, 2007, Probe for measuring groundwater velocity at the centimeter
780 scale. *Environmental Science and Technology*, volume 41, number 24, pages 8453-8458.
- 781 Lee, J., Kitanidis, P.K., 2014. Large-scale hydraulic tomography and joint inversion of head and tracer
782 data using the principal component geostatistical approach (PCGA). *Water Resour. Res.* 50, 5410–
783 5427.
- 784 Lee, J., Kokkinaki, A., Kitanidis, P.K., 2018. Fast large-scale joint inversion for deep aquifer
785 characterization using pressure and heat tracer measurements. *Transp. Porous Media* 123, 533–
786 543.
- 787 Lee, J., Yoon, H., Kitanidis, P.K., Werth, C.J., Valocchi, A.J., 2016. Scalable subsurface inverse modeling of
788 huge data sets with an application to tracer concentration breakthrough data from magnetic

- 789 resonance imaging. *Water Resour. Res.* 52, 5213–5231.
- 790 Lie, K.-A., 2019. An introduction to reservoir simulation using MATLAB/GNU Octave: User guide for the
791 MATLAB Reservoir Simulation Toolbox (MRST). Cambridge University Press.
- 792 Liu, F., Yeh, T.J., Wang, Y., Hao, Y., Wen, J., Wang, W., 2020. Characterization of basin-scale aquifer
793 heterogeneity using transient hydraulic tomography with aquifer responses induced by
794 groundwater exploitation reduction. *J. Hydrol.* 588, 125137.
795 <https://doi.org/10.1016/j.jhydrol.2020.125-137>
- 796 Liu, S., Yeh, T.J., Gardiner, R., 2002. Effectiveness of hydraulic tomography: Sandbox experiments. *Water*
797 *Resour. Res.* 38, 1–5.
- 798 Liu, X., Illman, W.A., Craig, A.J., Zhu, J., Yeh, T., 2007. Laboratory sandbox validation of transient
799 hydraulic tomography. *Water Resour. Res.* 43(5).
- 800 Lochbühler, T., Doetsch, J., Brauchler, R., Linde, N., 2013. Structure-coupled joint inversion of
801 geophysical and hydrological data. *Geophysics* 78, ID1–ID14.
- 802 Luo, N., Illman, W.A., Zha, Y., Park, Y.-J., Berg, S.J., 2020. Three-dimensional hydraulic tomography
803 analysis of long-term municipal wellfield operations: Validation with synthetic flow and solute
804 transport data. *J. Hydrol.* 590, 125438.
- 805 Luo, N., Zhao, Z., Illman, W.A., Berg, S.J., 2017. Comparative study of transient hydraulic tomography
806 with varying parameterizations and zonations: Laboratory sandbox investigation. *J. Hydrol.* 554,
807 758–779.
- 808 Maldaner, C.H., Munn, J.D., Coleman, T.I., Molson, J.W., Parker, B.L., 2019. Groundwater flow
809 quantification in fractured rock boreholes using active distributed temperature sensing under
810 natural gradient conditions. *Water Resour. Res.* 55, 3285–3306.
- 811 Mao, D., Yeh, T.-C.J., Wan, L., Hsu, K.-C., Lee, C.-H., Wen, J.-C., 2013. Necessary conditions for inverse
812 modeling of flow through variably saturated porous media. *Adv. Water Resour.* 52, 50–61.
- 813 Michael Tso, C., Zha, Y., Jim Yeh, T., Wen, J., 2016. The relative importance of head, flux, and prior
814 information in hydraulic tomography analysis. *Water Resour. Res.* 52, 3–20.
- 815 Paradis, D., Gloaguen, E., Lefebvre, R., Giroux, B., 2015. Resolution analysis of tomographic slug test

- 816 head data: Two-dimensional radial case. *Water Resour. Res.* 51, 2356–2376.
- 817 Paradis, D., Lefebvre, R., Gloaguen, E., Giroux, B., 2016. Comparison of slug and pumping tests for
818 hydraulic tomography experiments: a practical perspective. *Environ. Earth Sci.* 75(16), 1159.
- 819 Read, T., Bour, O., Selker, J.S., Bense, V.F., Le Borgne, T., Hochreutener, R., Lavenant, N., 2014. Active-
820 distributed temperature sensing to continuously quantify vertical flow in boreholes. *Water Resour.*
821 *Res.* 50, 3706–3713.
- 822 Revil, A., Karaoulis, M., Johnson, T., Kemna, A., 2012. Some low-frequency electrical methods for
823 subsurface characterization and monitoring in hydrogeology. *Hydrogeol. J.* 20, 617–658.
- 824 Sayde, C., Thomas, C.K., Wagner, J., Selker, J., 2015. High-resolution wind speed measurements using
825 actively heated fiber optics. *Geophys. Res. Lett.* 42, 10–64.
- 826 Schneider, H.A., Jackson, W.A., Rainwater, K., Reible, D., Morse, S., Hatzinger, P.B., Garza-Rubalcava, U.,
827 2019. Estimation of Interstitial Velocity Using a Direct Drive High-Resolution Passive Profiler.
828 *Groundwater* 57, 915–924.
- 829 Simon, N., Bour, O., Lavenant, N., Porel, G., Nauleau, B., Pouladi, B., Longuevergne, L. (2020). A
830 Comparison of Different Methods to Estimate the Effective Spatial Resolution of FO-DTS
831 Measurements Achieved during Sandbox Experiments. *Sensors*, 20(2).
832 <https://doi.org/10.3390/s20020570>
- 833 Simon, N., Bour, O., Lavenant, N., Porel, G., Nauleau, B., Pouladi, B., Longuevergne, L., & Crave, A.
834 (2021). Numerical and Experimental Validation of the Applicability of Active-DTS Experiments to
835 Estimate Thermal Conductivity and Groundwater Flux in Porous Media. *Water Resources Research*,
836 57(1), e2020WR028078. <https://doi.org/10.1029/2020WR028078>
- 837 Slater, L., 2007. Near surface electrical characterization of hydraulic conductivity: From petrophysical
838 properties to aquifer geometries—A review. *Surv. Geophys.* 28, 169–197.
- 839 Somogyvári, M., Bayer, P., 2017. Field validation of thermal tracer tomography for reconstruction of
840 aquifer heterogeneity. *Water Resour. Res.* 53, 5070–5084.
- 841 Soueid Ahmed, A., Jardani, A., Revil, A., Dupont, J.-P., 2016. Joint inversion of hydraulic head and self-
842 potential data associated with harmonic pumping tests. *Water Resour. Res.* 52, 6769–6791.

- 843 Sun, R., Yeh, T.J., Mao, D., Jin, M., Lu, W., Hao, Y., 2013. A temporal sampling strategy for hydraulic
844 tomography analysis. *Water Resour. Res.* 49, 3881–3896.
- 845 Tiedeman, C.R., Barrash, W., 2020. Hydraulic tomography: 3D hydraulic conductivity, fracture network,
846 and connectivity in mudstone. *Groundwater* 58, 238–257.
- 847 Tosaka, H., Masumoto, K., Kojima, K., 1993. Hydropulse tomography for identifying 3-D permeability
848 distribution, in: *High Level Radioactive Waste Management: Proceedings. Volume 1*, 955-959
- 849 Yeh, T.-C., Khaleel, R., Carroll, K.C., 2015. *Flow through heterogeneous geologic media*. Cambridge
850 University Press.
- 851 Yeh, T.J., Liu, S., 2000. Hydraulic tomography: Development of a new aquifer test method. *Water*
852 *Resour. Res.* 36, 2095–2105.
- 853 Yin, D., Illman, W.A., 2009. Hydraulic tomography using temporal moments of drawdown recovery data:
854 A laboratory sandbox study. *Water Resour. Res.* 45(1).
- 855 Zha, Y., Yeh, T.-C.J., Mao, D., Yang, J., Lu, W., 2014a. Usefulness of flux measurements during hydraulic
856 tomographic survey for mapping hydraulic conductivity distribution in a fractured medium. *Adv.*
857 *Water Resour.* 71, 162–176.
- 858 Zha, Y., Yeh, T.J., Illman, W.A., Onoe, H., Mok, C.M.W., Wen, J., Huang, S., Wang, W., 2017. Incorporating
859 geologic information into hydraulic tomography: A general framework based on geostatistical
860 approach. *Water Resour. Res.* 53, 2850–2876.
- 861 Zha, Y., Yeh, T.J., Illman, W.A., Zeng, W., Zhang, Y., Sun, F., Shi, L., 2018. A reduced-order successive
862 linear estimator for geostatistical inversion and its application in hydraulic tomography. *Water*
863 *Resour. Res.* 54, 1616–1632.
- 864 Zha, Y., Yeh, T.J., Mao, D., Yang, J., Lu, W., 2014b. *Advances in Water Resources* Usefulness of flux
865 measurements during hydraulic tomographic survey for mapping hydraulic conductivity
866 distribution in a fractured medium. *Adv. Water Resour.* 71, 162–176.
867 <https://doi.org/10.1016/j.advwatres.2014.06.008>
- 868 Zhao, Z., Illman, W.A., 2021. On the importance of considering specific storage heterogeneity in
869 hydraulic tomography: Laboratory sandbox and synthetic studies. *J. Hydrol.* 593, 125874.

- 870 Zhao, Z., Illman, W.A., 2018. Three-dimensional imaging of aquifer and aquitard heterogeneity via
871 transient hydraulic tomography at a highly heterogeneous field site. *J. Hydrol.* 559, 392–410.
- 872 Zhao, Z., Illman, W.A., Berg, S.J., 2016. On the importance of geological data for hydraulic tomography
873 analysis: Laboratory sandbox study. *J. Hydrol.* 542, 156–171.
- 874 Zhu, J., Yeh, T.-C.J., 2005. Characterization of aquifer heterogeneity using transient hydraulic
875 tomography. *Water Resour. Res.* 41(7).
- 876

Journal Pre-proof